

AD-A141 785

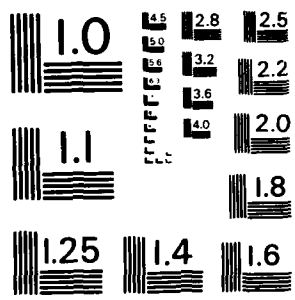
DESIGN OF INCIDENT FIELD B-DOT SENSOR FOR THE NOSE BOOM 1 / 1
OF NASA F-108B AIRCRAFT(U) DIKEWOOD ALBUQUERQUE NM
D V GIRI ET AL. APR 84 AFWL-TR-83-141 F29801-82-C-0027

UNCLASSIFIED

F/G 14/2

NL

END
DATE
FILED
7 84
PTO



MICROCOPY RESOLUTION TEST CHART
NATIONAL BUREAU OF STANDARDS-1963-A

AFWL-TR-83-141

2

AFWL-TR-83-141

AD-A141 765

DESIGN OF INCIDENT FIELD B-DOT SENSOR FOR THE NOSE BOOM OF NASA F-106B AIRCRAFT

David V. Gir
Stuart H. Sands

LuTech, Inc.
3516 Breakwater Ct
Hayward CA 94545

April 1984

Final Report



Approved for public release; distribution unlimited.

DTIC FILE COPY

DTIC
ELECTE
JUN 4 1984
S B

AIR FORCE WEAPONS LABORATORY
Air Force Systems Command
Kirtland Air Force Base, NM 87117

84 06 04 048

AFWL-TR-83-141

This final report was prepared by LuTech Incorporated, Hayward, California, under Contract F29601-82-C-0027, Job Order 37630131 with the Air Force Weapons Laboratory, Kirtland Air Force Base, New Mexico. First Lieutenant Dennis J. Andersh (NTAA) was the Laboratory Project Officer-in-Charge.

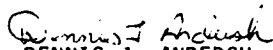
When Government drawings, specifications, or other data are used for any purpose other than in connection with a definitely Government-related procurement, the United States Government incurs no responsibility or any obligation whatsoever. The fact that the Government may have formulated or in any way supplied the said drawings, specifications, or other data, is not to be regarded by implication, or otherwise in any manner construed, as licensing the holder, or any other person or corporation; or as conveying any rights or permission to manufacture, use, or sell any patented invention that may in any way be related thereto.

This report has been authored by a contractor of the United States Government. Accordingly, the United States Government retains a nonexclusive, royalty-free license to publish or reproduce the material contained herein, or allow others to do so, for the United States Government purposes.

This report has been reviewed by the Public Affairs Office and is releasable to the National Technical Information Service (NTIS). At NTIS, it will be available to the general public, including foreign nations.

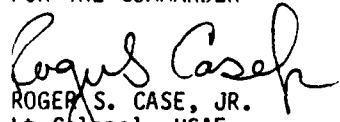
If your address has changed, if you wish to be removed from our mailing list, or if your organization no longer employs the addressee, please notify AFWL/NTAA, Kirtland AFB, NM 87117 to help us maintain a current mailing list.

This technical report has been reviewed and is approved for publication.


DENNIS J. ANDERSH
1Lt, USAF
Project Officer


DAVID W. GARRISON
Lt Colonel, USAF
Chief, Applications Branch

FOR THE COMMANDER


ROGER S. CASE, JR.
Lt Colonel, USAF
Chief, Aircraft and Missiles Division

DO NOT RETURN COPIES OF THIS REPORT UNLESS CONTRACTUAL OBLIGATIONS OR NOTICE ON A SPECIFIC DOCUMENT REQUIRES THAT IT BE RETURNED.

UNCLASSIFIED

SECURITY CLASSIFICATION OF THIS PAGE

REPORT DOCUMENTATION PAGE				
1a. REPORT SECURITY CLASSIFICATION Unclassified		1b. RESTRICTIVE MARKINGS		
2a. SECURITY CLASSIFICATION AUTHORITY		3. DISTRIBUTION/AVAILABILITY OF REPORT Approved for public release; distribution unlimited.		
2b. DECLASSIFICATION/DOWNGRADING SCHEDULE		4. PERFORMING ORGANIZATION REPORT NUMBER(S)		
4. PERFORMING ORGANIZATION REPORT NUMBER(S)		5. MONITORING ORGANIZATION REPORT NUMBER(S) AFWL-TR-83-141		
6a. NAME OF PERFORMING ORGANIZATION LuTech, Inc.	6b. OFFICE SYMBOL (If applicable)	7a. NAME OF MONITORING ORGANIZATION Air Force Weapons Laboratory		
6c. ADDRESS (City, State and ZIP Code) 3516 Breakwater Ct Hayward CA 94545		7b. ADDRESS (City, State and ZIP Code) Kirtland Air Force Base, NM 87117		
8a. NAME OF FUNDING/SPONSORING ORGANIZATION	8b. OFFICE SYMBOL (If applicable)	9. PROCUREMENT INSTRUMENT IDENTIFICATION NUMBER F29601-82-C-0027		
8c. ADDRESS (City, State and ZIP Code)		10. SOURCE OF FUNDING NOS.		
		PROGRAM ELEMENT NO. 64711F	PROJECT NO. 3763	TASK NO. 01
				WORK UNIT NO. 31
11. TITLE (Include Security Classification) DESIGN OF INCIDENT FIELD B-DOT SENSOR FOR THE NOSE BOOM OF NASA F-106B AIRCRAFT				
12. PERSONAL AUTHOR(S) Giri, David V.; Sands, Stuart H.				
13a. TYPE OF REPORT Final	13b. TIME COVERED FROM 83 Jun to 83 Dec	14. DATE OF REPORT (Yr, Mo, Day) 1984 April	15. PAGE COUNT 71	
16. SUPPLEMENTARY NOTATION This work was performed by LuTech, Inc., under Subtask 03-03, Subcontract DC-SC-1026-4, for Dikewood, Div of Kaman Sciences Corp., 1613 Univ Blvd NE, Albuquerque, NM 87102.				
17. COBALT CODES		18. SUBJECT TERMS (Continue on reverse if necessary and identify by block number)		
FIELD	GROUP	SUB. GR.		
		Boom Sensor, EM Measurement, F-106B Aircraft, Incident Field		
19. ABSTRACT (Continue on reverse if necessary and identify by block number)				
This report deals specifically with the design considerations of including a B-dot sensor on the existing nose boom of the NASA Langley Research Center experimental F-106B aircraft. Although mounting the B-dot sensor on the existing boom may not be the ideal location, time and aerodynamic constraints require a consideration of sensor placement on the boom. This report also analyzes the performance of a B-dot sensor on the existing boom. The objective of the B-dot sensor is to enable a measurement of the incident B-dot field in the direction of the aircraft axis, in a flyby configuration near the ATHAMAS II (VPD-II) facility. Selected scale-model data useful in supporting the sensor design are included in Appendix B.				
20. DISTRIBUTION/AVAILABILITY OF ABSTRACT UNCLASSIFIED/UNLIMITED <input checked="" type="checkbox"/> SAME AS RPT. <input type="checkbox"/> DTIC USERS <input type="checkbox"/>		21. ABSTRACT SECURITY CLASSIFICATION Unclassified		
22a. NAME OF RESPONSIBLE INDIVIDUAL 1Lt Dennis J. Andersh		22b. TELEPHONE NUMBER (Include Area Code) (505) 844-0326	22c. OFFICE SYMBOL NTAA	

DD FORM 1473, 83 APR

EDITION OF 1 JAN 73 IS OBSOLETE.

UNCLASSIFIED
SECURITY CLASSIFICATION OF THIS PAGE

SUMMARY

This report has addressed the problem of designing a mast mountable Multi-Gap Loop (MGL) sensor for measurement of an incident magnetic field on an aircraft. Specifically, the proposed MGL-2E (AM) sensor is based on the available design of MGL-2B (A) sensor to be mounted on the pitot-static nose boom of the NASA F-106B research aircraft. Given the time and physical constraints, this design was undertaken to study the feasibility of adding a sensor to the existing nose boom. Besides the electromagnetic consideration, several other factors of mechanical, flight critical, and aerodynamic nature have to be accommodated in such a design. From an electromagnetic point of view, conservative error estimates are obtained for the various sensor placement options considered. In estimating these errors, the worst-case polarization of E vector parallel to wings, with H vector parallel to the aircraft axis, is considered. This case does not correspond to the flyby configurations; consequently, the errors obtained in actual measurement may in some cases be smaller than estimated. Furthermore, for each sensor placement option, mechanical and aerodynamic aspects are also evaluated and tabulated for comparison.

The objective of this report is to provide useful inputs to personnel involved in the manufacturing and installation of the proposed sensor. Precision of dimensions has not been attempted and refinements upon this design will probably be necessary and are welcome.

PREFACE

Several individuals at various Govt. agencies and in industry have helped in the preparation of this report. The authors wish to thank Dr. Carl E. Baum and Lt. Dennis Andersh of the Air Force Weapons Laboratory for valuable discussions. Mr. Felix Pitts, Bruce Fischer, and Norm Crabill of NASA Langley Research Center have cooperated by providing useful information about the aircraft, the boom, and flight requirements. The authors are also thankful to Mr. Gary Sower of EG&G, Albuquerque, for discussions regarding the commercially available B-dot sensors, and to Dr. Kelvin Lee of Dikewood Division of Kaman Sciences for constant support during the course of this work.

CONTENTS

<u>Section</u>		<u>Page</u>
I	INTRODUCTION	7
	1. SCATTERING BY FUSELAGE	8
	2. ANTISYMMETRIC COUPLING FROM THE DELTA WINGS	10
	3. HIGH-FREQUENCY ANTISYMMETRIC ERRORS	15
	4. ERROR ESTIMATES	17
II	B-DOT SENSOR DESIGN	19
	1. DESIGN CONSTRAINTS	19
	2. CHOICE OF SENSOR FROM AVAILABLE DESIGNS	22
	3. SENSOR MODIFICATIONS	22
	4. PLACEMENT OF SENSOR	26
III	EXPECTED B, B-DOT, AND SENSOR OUTPUT VOLTAGE DURING FLYBY	32
IV	CONCLUSIONS AND RECOMMENDATIONS	52
	APPENDICES	
	A. INVESTIGATION OF VARIOUS FUSELAGE SCATTERING MODELS	55
	B. SELECTED DATA FROM SCALE-MODEL MEASUREMENT	59

Accession For	
NTIS GRA&I	<input checked="" type="checkbox"/>
DTIC TAB	<input type="checkbox"/>
Unannounced	<input type="checkbox"/>
Justification	
By _____	
Distribution/	
Availability Codes	
Dist	Avail and/or Special
A-1	

ILLUSTRATIONS

<u>Figure</u>	<u>Page</u>
1 Geometry of the scatterer	9
2 Side view of the F-106B aircraft	11
3 Fitting the scatterer model to the aircraft	12
4 Top view of the F-106B aircraft	13
5 Scattering model for estimating the wing coupling	14
6 Geometry for estimating the high-frequency scattering errors	16
7 Metal components in radome of NASA F-106B storm hazards research airplane (side view) [Provided by M. Klebitz of NASA Langley Research Center]	20
8 Internal view of MGL-2B (A) sensor	23
9 Internal view of proposed MGL-2E (AM) sensor accommodating the F-106B pitot-static boom	23
10 Design details of B-dot sensor [MGL-2E (AM)] based on available MGL-2B (A) data	25
11 The radome and pitot-static boom of the F-106B aircraft	27
12 Various options of sensor placement	28
13 Locations used in computing cB_{ϕ} and \dot{B}_{ϕ} for the VPD II facility.	35
14 Computed cB_{ϕ} (kV/m) at different heights for $\psi = 173.2$ m from the VPD II apex	36
15 Computed cB_{ϕ} (kV/m) at different heights for $\psi = 304$ m from the VPD II apex	37
16 Computed cB_{ϕ} (kV/m) at different heights for $\psi = 439.3$ m from the VPD II apex	38
17 Computed cB_{ϕ} (kV/m) at different heights for $\psi = 624.1$ m from the VPD II apex	39
18 Computed cB_{ϕ} (kV/m) at different heights for $\psi = 608$ m from the VPD II apex	40
19 Computed cB_{ϕ} (kV/m) at different heights for $\psi = 878.6$ m from the VPD II apex	41

ILLUSTRATIONS (Continued)

<u>Figure</u>		<u>Page</u>
20	Computed cB_{ϕ} (kV/m) at different heights for $\psi = 1248.2$ m from the VPD II apex	42
21	Computed cB_{ϕ} (kV/m) at different heights for $\psi = 1600$ m from the VPD II apex	43
22	Computed \dot{B}_{ϕ} (kV/m^2) and sensor output voltage V_s (Volts) assuming $A_{eq} = 10^{-2} m^2$ for distance $\psi = 173.2$ m from the VPD II apex	44
23	Computed \dot{B}_{ϕ} (kV/m^2) and sensor output voltage V_s (Volts) assuming $A_{eq} = 10^{-2} m^2$ for distance $\psi = 439.3$ m from the VPD II apex	45
24	Computed \dot{B}_{ϕ} (kV/m^2) and sensor output voltage V_s (Volts) assuming $A_{eq} = 10^{-2} m^2$ for distance $\psi = 304$ m from the VPD II apex	46
25	Computed \dot{B}_{ϕ} (kV/m^2) and sensor output voltage V_s (Volts) assuming $A_{eq} = 10^{-2} m^2$ for distance $\psi = 624.1$ m from the VPD II apex	47
26	Computed \dot{B}_{ϕ} (kV/m^2) and sensor output voltage V_s (Volts) assuming $A_{eq} = 10^{-2} m^2$ for distance $\psi = 608$ m from the VPD II apex	48
27	Computed \dot{B}_{ϕ} (kV/m^2) and sensor output voltage V_s (Volts) assuming $A_{eq} = 10^{-2} m^2$ for distance $\psi = 878.6$ m from the VPD II apex	49
28	Computed \dot{B}_{ϕ} (kV/m^2) and sensor output voltage V_s (Volts) assuming $A_{eq} = 10^{-2} m^2$ for distance $\psi = 1248.2$ m from the VPD II apex	50
29	Computed \dot{B}_{ϕ} (kV/m^2) and sensor output voltage V_s (Volts) assuming $A_{eq} = 10^{-2} m^2$ for distance $\psi = 1600$ m from the VPD II apex	51

ILLUSTRATIONS (Concluded)

<u>Figure</u>		<u>Page</u>
A1	A model for quasi-magnetostatic scattering (side view)	57
A2	A model for quasi-magnetostatic scattering (top view)	57
A3	A model for quasi-magnetostatic scattering (side view)	57
A4	A model for quasi-magnetostatic scattering (top view)	57
B1	Nose-on incidence in scale-model measurements	60
B2	The observation points relative to bulkhead	60
B3	Measured field H_{z0} without the aircraft	61
B4	Measured field H_{z1} with the aircraft	61
B5	The mean error, ϵ_r , measured with a vertical ground plane oriented normal to the incident electric field	63
B6	Positions of test points used in scale-model measurements	65
B7	Errors for the right side incidence, E parallel to vertical stabilizer	66
B8	Errors for top incidence, E perpendicular to fuselage	67

TABLES

<u>Table</u>		<u>Page</u>
1	Physical quantities of interest with different positioning of the MGL-2E (AM) B-dot sensor	31
A1	Fuselage scattering errors for the different models and options discussed in the text	58

I. INTRODUCTION

The objective of this report is to describe the design considerations of an incident B-dot field sensor to be mounted on the existing pitot-static boom of the NASA Langely Research Center F-106B aircraft. The B-dot sensor is intended for the measurement of an incident magnetic field using the aircraft as a platform in such a way that the scattered field from the aircraft does not impact the measurement. The electromagnetic considerations of placing a B-dot sensor in both forward and aft sections of any aircraft were considered in detail in Reference 1. The electromagnetic considerations are obviously aircraft specific, because of structural variations. This report examines in detail the various possible options in including a B-dot sensor to the existing NASA F-106B pitot-static boom. Each option is considered and its electromagnetic and mechanical characteristics are evaluated for comparison. It is expected that this report will provide useful information to the personnel involved in actual fabrication and installation of the sensor on the boom.

A chief consideration in the design of a B-dot sensor to be mounted on the nose boom of an F-106B aircraft is the estimation of scattered field pickup. Since the object is to measure the incident axial magnetic field, the sensor should be placed and oriented to minimize its sensitivity to the scattered field. In addition to the incident field, the sensor can respond to axial components of

- quasi-magnetostatic antisymmetric fields scattered by fuselage
- antisymmetric coupling from the delta wings

1. Giri, D.V. and Baum, C.E., "Airborne Platform for Measurement of Transient or Broadband CW Electromagnetic Fields," Air Force Weapons Laboratory, Kirtland Air Force Base, NM, Sensor and Simulation Note (to be published).

- high-frequency antisymmetric errors.

The necessary equations in estimating the above parameters will first be individually summarized below and then applied specifically to the F-106B aircraft.

1. SCATTERING BY FUSELAGE

Figure 1 shows a cigar-shaped model of the fuselage for which quasimagnetostatic scattered fields on the axis were derived in Reference 2. If H_0 is the axial incident field to be measured, b is the radius of the sensing loop, and a is the radius of fuselage, then the ratio of scattered to incident field on the axis is given in Reference 2 as

$$\frac{H_z^{(\text{scat})}}{H_z^{(\text{inc})}} = -\frac{a^2}{2b^2} \left\{ 1 - \frac{1}{\sqrt{1 + (b/z_0)^2}} \right\} \quad (1)$$

The above ratio, which is an error estimate, can be shown to be

$$\frac{H_z^{(\text{scat})}}{H_z^{(\text{inc})}} \approx -\frac{1}{4} \left(\frac{a^2}{z_0^2} \right) \quad \text{if } (b \ll z_0) \quad (2)$$

Note that the above expression is an error estimate if the sensor is located along the axis where both the scattered and incident fields are axial, with the radial component of scattered field vanishing. Also note that, in the analytical model of Figure 1, the origin of coordinates, from where the axial distance z_0 is measured, is half a radius (0.5 a) inward from the metallic scatterer.

2. Latham, R.W. and Lee, K.S.H., "Magnetic Field Distortion by a Specific Axisymmetric, Semi-infinite, Perfectly Conducting Body," Air Force Weapons Laboratory, Kirtland Air Force Base, NM, Sensor and Simulation Note 102, April 1970.

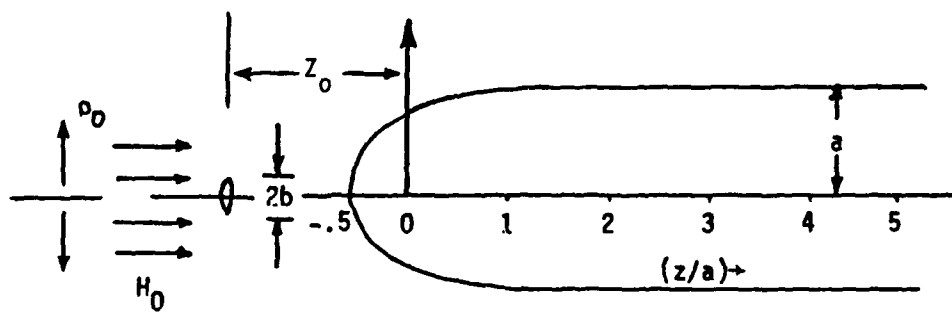


Figure 1. Geometry of the scatterer.

Figure 2 shows the side view of the F-106B aircraft along with the major dimensions. In Figure 3 the analytical model is fitted to the aircraft at the bulkhead. In this fit, observe that if the B-dot sensing loop is placed on the existing boom, it is below the axis of the analytical model of the aircraft, pointing out a need for an expression for the error estimate off the axis. This was considered in Reference 1 and is given by:

$$\Delta_f = \frac{H_z^{(\text{scat})}}{H_z^{(\text{inc})}} = -\frac{a^2}{2b^2} \left[\frac{z}{\sqrt{\rho_0^2 + z_0^2}} - \frac{z}{\sqrt{(\rho_0 + b)^2 + z_0^2}} \right] \quad (3)$$

where ρ_0 is the radial offset of the sensing loop in the symmetry plane. Observe that on the axis, $\rho_0 = 0$, and Equation 3 reduces to Equation 1. Furthermore, when the sensing loop is off the axis, there is a radial component of the scattered field due to the fuselage, but the orientation of the sensing loop is such that it is insensitive to the radial scattered field. In conclusion, Equation 3 will be used in estimating the error due to fuselage scattering.

2. ANTISYMMETRIC COUPLING FROM THE DELTA WINGS

Figure 4 shows the top view of the F-106B aircraft from which the delta wing dimensions are extracted and shown in Figure 5. The delta wing, for purposes of estimating low-frequency scattering, is approximated by a rectangular plate of the same area centrally located. Since the sensor must be placed on the existing nose boom, this central location of the rectangular plate model of the delta wing leads to a conservative estimate of the error due to antisymmetric wing coupling. The rectangular plate can then be modeled by (Ref. 3) a conducting post of equivalent radius ($a_{\text{eq}} = \text{plate width}/4$) as shown in Figure 5. If the conducting post model is used, the magnetic field due to wing current does not have a component along the

3. Jasik, H., Editor Antenna Engineering Handbook, Chapter 3, McGraw Hill, 1961.

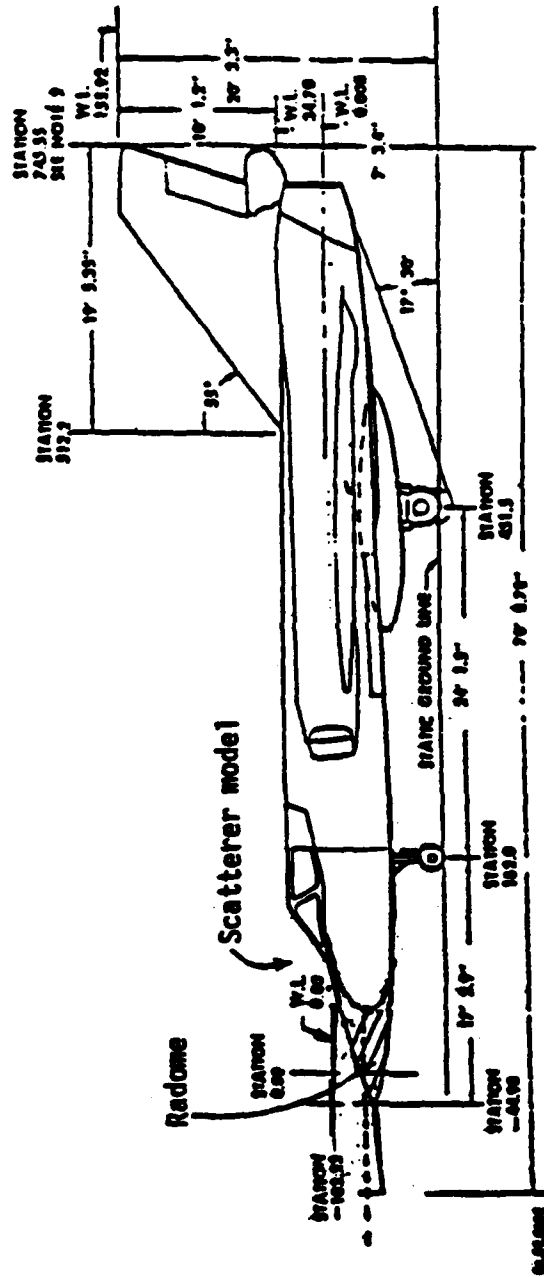


Figure 3. Fitting the scatterer model to the aircraft.

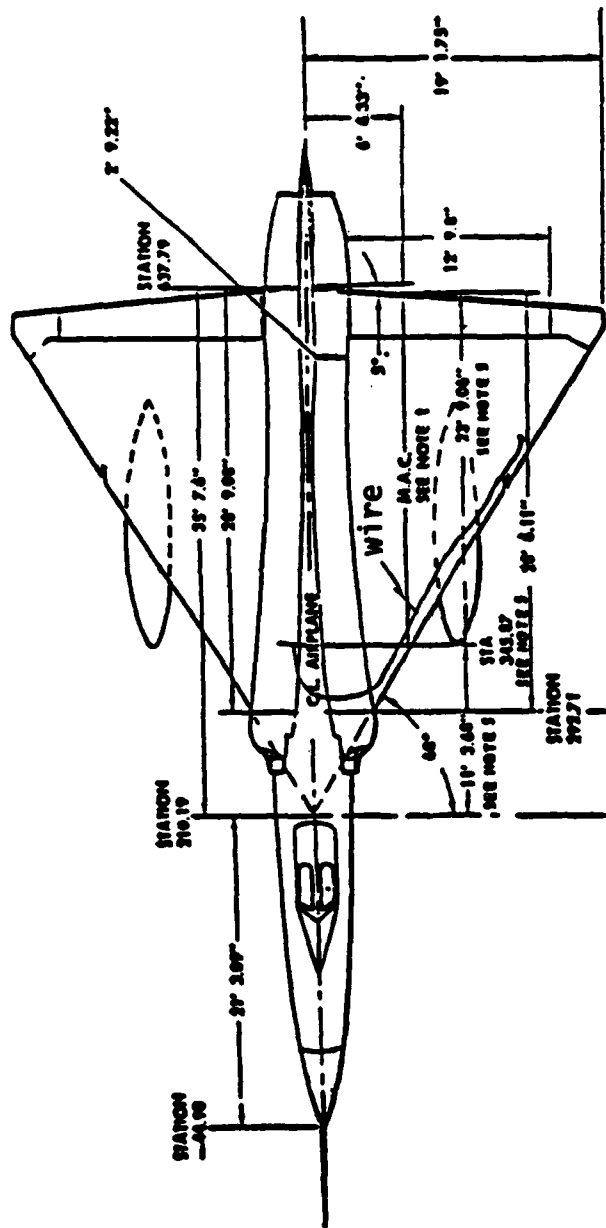


Figure 4. Top view of F-106B aircraft.

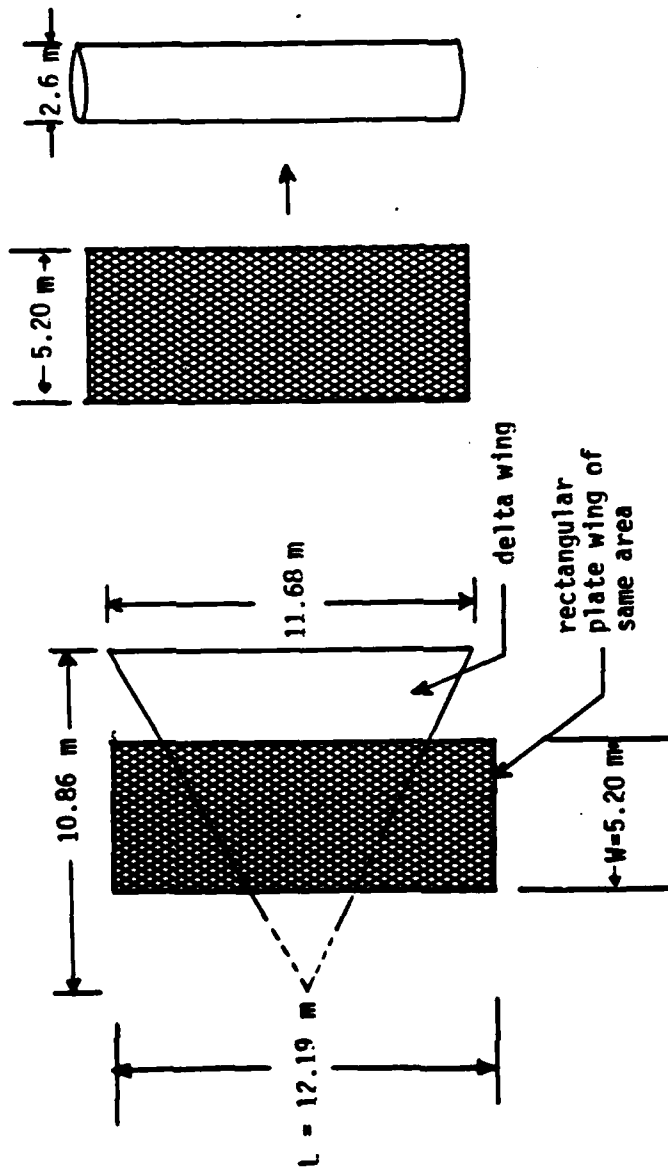


Figure 5. Scattering model for estimating the wing coupling.

fuselage axis. Using the results of Reference 4 and correcting it for the wing thickness, an upper bound on the error due to wing scattering can be estimated by using

$$\begin{aligned} \Delta_w &= \text{error due to wing coupling} = \left| \frac{H_z^{(\text{scat})}}{H_z^{(\text{inc})}} \right| \\ &\approx \frac{h}{R} \times \frac{t}{R} \end{aligned} \quad (4)$$

where $2h$ = wing span, $2t$ = wing thickness, and R = distance of sensor from wing. In Equation 4 above, the (h/R) term comes from earlier calculations (Fig. 5 of Ref. 4) and the factor t/R is the correction due to wing thickness. Note that this expression gives an upper bound of the error at the frequency corresponding to antisymmetric wing resonance. The error is lower below and above this resonant frequency. Equation 4 is later used in this report to get the error estimate due to antisymmetric wing scattering.

3. HIGH-FREQUENCY ANTISYMMETRIC ERRORS

Figure 6 shows the geometry for estimating the errors due to high-frequency scattering. The scattered magnetic field per unit incident field has an axial component, and is indicative of the error, due to high frequency scattering. It is given by

$$\Delta_h = \text{high-frequency error} = \left| \frac{H_z^{(\text{scat})}}{H_z^{(\text{inc})}} \right| \quad (5)$$

$$\approx \sin(\alpha) \times \text{diffraction coefficient} \times \text{propagation factor}$$

4. Sassman, R.W., Latham, R.W. and Berger, A.G., "Electromagnetic Scattering from a Conducting Post," Air Force Weapons Laboratory, Kirtland Air Force Base, NM, Sensor and Simulator Note 45, June 1967.

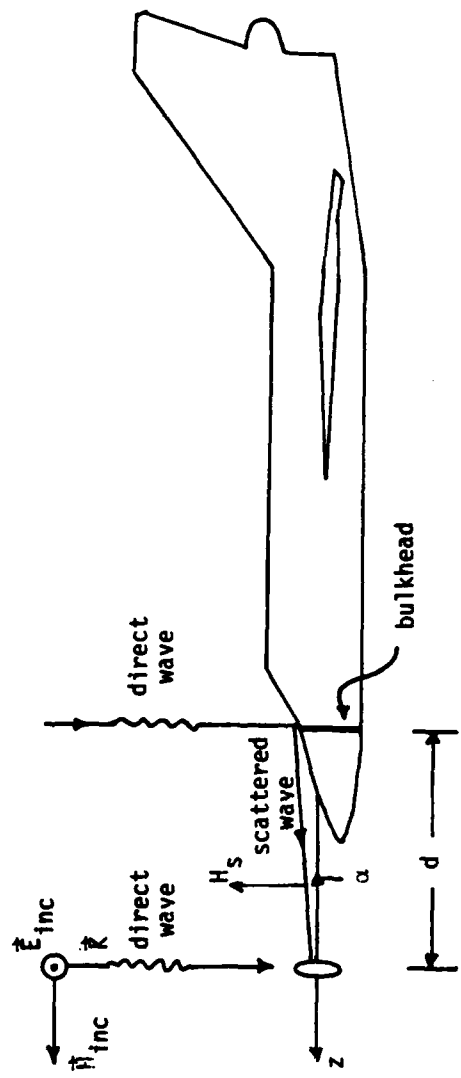


Figure 6. Geometry for estimating the high-frequency scattering errors.

The diffraction coefficient times propagation factor has been approximated to be unity in this estimation, in order to get conservative error estimates.

4. ERROR ESTIMATES

The three different categories of error estimates, Δ_f , Δ_w , and Δ_h , for which expressions are given above, are used in evaluating the various options for sensor placement.

In addition to the above outlined electromagnetic requirement for sensor placement, other considerations are:

- interference from weather radar in the radome on the sensor performance
- interference from the presence of the sensor on radar performance
- interaction with pitot-static tube
- impact of sensor weight on existing boom
- modification of boom for sensor cable routing
- aerodynamic compatibility
- impact on α and β flow vanes on existing boom

The remainder of this report is organized as follows. All of the above considerations, i.e., electromagnetic, mechanical, and aerodynamic, are discussed in Section II. Four possible sensor locations are proposed and evaluated in Section II, and results are presented in tabular form at the end of the section. In Section III, computation of expected B , $B\text{-dot}$ and V_{sensor} are presented, for various flight patterns over the AFWL VPD-II simulator. Relevant conclusions and recommendations are presented in

Section IV, which is followed by two Appendices. Appendix A investigates various scattering models for the fuselage that may be used in estimating the errors in the measurement of incident magnetic field due to fuselage scattering. Selected data from the scale-model measurements are included in Appendix B.

II. B-DOT SENSOR DESIGN

As noted in Section I, several considerations put constraints on both the design and placement of an incident B-dot sensor. Concerning the design of the sensor, after examining the available MGL (Multi Gap Loop) sensors, the proposed design was based on available data for the MGL-2B (A) sensor. The proposed sensor, whose design is based on the MGL-2B (A) sensor, has been called the MGL-2E (AM). The nomenclature conforms to the conventional MGL series with AM in parentheses denoting axial output while mast-mounted. The required changes to go from MGL-2B (A) to MGL-2E (AM) are considered in this section. Also, four possible locations for sensor placement are considered and evaluated in this section.

1. DESIGN CONSTRAINTS

Various considerations that impact the design and placement of sensors are individually discussed below.

a. Effect of weather radar on sensor--Figure 7, provided by NASA Langley Research Center, shows the metallic components present in the radome of NASA F-106B research aircraft. The weather radar antenna is mounted on the front face of the box-like radar package shown in Figure 7. Given the size of the radar package and antenna (~roughly a third of the diameter of the bulkhead to which the radome is attached), and given that the sensor is slightly over a fuselage diameter away from the radar package, the quasi-magnetostatic scattered fields from the radar package and antenna should not significantly contaminate the measured incident field. On the other hand, the existing six cables (viz., 2 heliax signal cables and 4 grounding straps) and the two additional cables from the B-dot sensor should be placed in a shielded enclosure such as a conducting pipe.

b. Effect of sensor on weather radar--The radar is horizontally polarized, i.e., its electric vector is out of the plane of the paper in

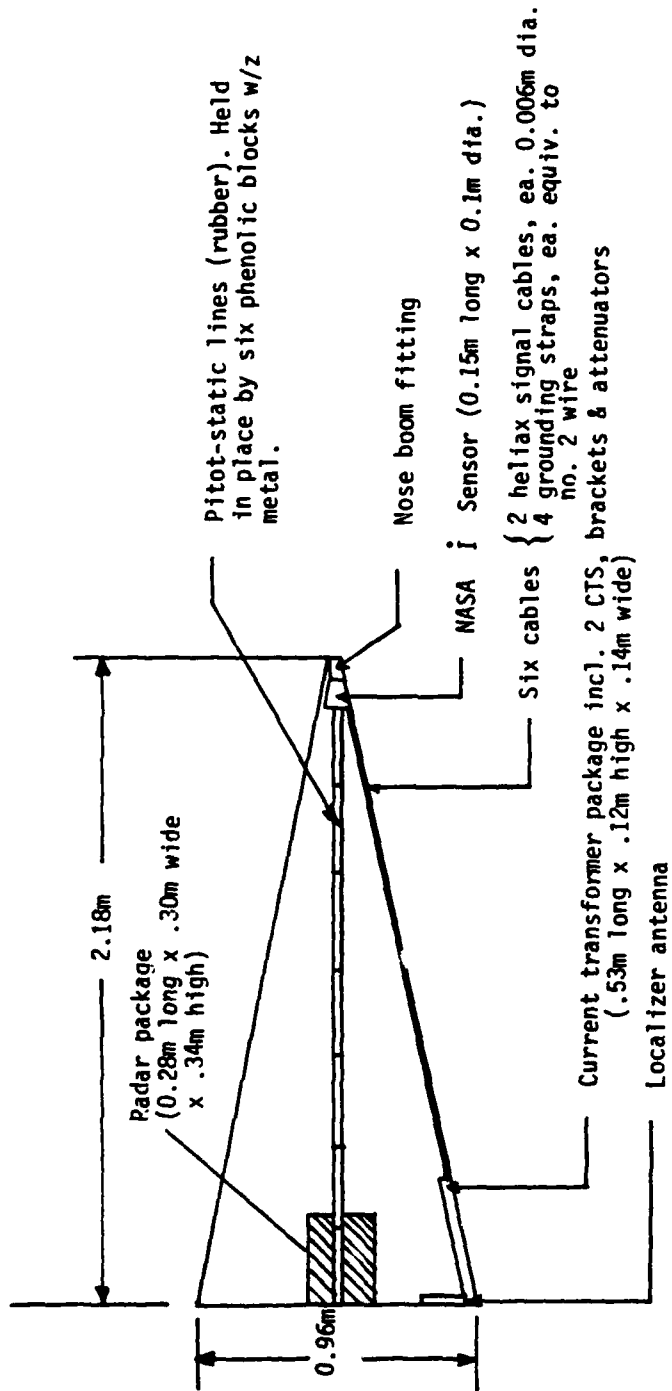


Figure 7. Metal components in radome of NASA F-106B storm hazards research airplane. (side view).
[Provided by Michael Klebitz of NASA Langley Research Center]

Figure 7. Also, the radar antenna axis is the same as the sensor axis. The horizontal shorting plate in the B-dot sensor, which is present to reduce the sensor sensitivity to electric fields, can affect the radar performance by shorting out the radar field, for a small range of angles on either side of the aircraft axis. In view of the fact that the weather radar need not necessarily be functional at the time of flyby near VPD II facility, no attempt has been made to quantify the effect of the presence of the sensor on the radar performance. An alternative proposal made by NASA Langley Research Center substitutes the radome from the inactive F-106A aircraft to the F-106B aircraft. It is felt that such a substitution is not warranted, especially if the weather radar is not operating during the planned simulator flyby tests in early 1984.

c. Interaction with pitot-static tube--The pitot-static tube at the end of the boom is a critical component for all flight missions, and the sensor placement should be such that the pitot-static tube is unobstructed and unaffected in its functioning at all times. This puts the sensor in the vicinity of α and β flow vanes. For the flyby test configuration, the α and β flow vanes are deemed unnecessary and could be removed without harming flight operations.

d. Impact of sensor weight on existing boom--It was estimated that the weight of the MGL-2E (AM) sensor is about 2.73 kg (6 lb). This is a rough estimate, and NASA personnel are studying the feasibility of adding such weight at the proposed sensor locations. It is anticipated that the sensor weight will restrict maximum "g-loading" of the aircraft.

e. Modification of boom for sensor placement--One possible way of fastening the proposed MGL-2E (AM) sensor to the boom is with 4 screws on either side, which together require 8 screw holes on the boom. In addition, 2 more holes (or one larger one) are required for routing the coaxial cables from the sensor into the boom. These 8 screw holes and cable access holes are the required modifications to the boom. The possibility of making use of existing screw holes on the boom has also been explored.

f. Aerodynamic compatibility--The sensor should present an aerodynamic profile that permits smooth air flow across it. This can be achieved by the addition of tapers or skirts to each end of the sensor. This is illustrated in Figure 10.

2. CHOICE OF SENSOR FROM AVAILABLE DESIGNS

For these measurements, a free-field B-dot sensor is needed which can be suitably modified for the specific needs of measuring an incident magnetic field. A generic type considered here is the Multi Gap Loop (MGL) type, which leaves one to evaluate MGL-1C (A), the MGL-2B (A), and the MGL-6A (A) sensors. The (A) signifies that the cables are axial, as opposed to radial, feed. All are made by EG&G. All the sensors operate on the same principle, the difference being in size, weight, and equivalent area. The MGL-1C (A) can be immediately ruled out due to its weight (18 kg) and size. The MGL-2B (A) weighs approximately 3 kg and the MGL-6A (A) weighs 0.5 kg. The equivalent area for the MGL-6A (A) is 10 times smaller than that of the MGL-2B (A) and it is only slightly larger in diameter than the boom, resulting in a significant loss of equivalent area. The cross-sectional area of the boom subtracts from the equivalent area of the sensor and hence, the MGL-6A (A) is unsuitable. Consequently, the proposed MGL-2E (AM) design is based on design data available (Ref. 5) on the MGL-2B (A) sensor.

3. SENSOR MODIFICATIONS

The internal view of the MGL-2B (A) sensor shown in Figure 8 has the following specifications:

Effective area	:	0.01 m ²
Rise time 10-90%	:	1.2 ns
Output	:	Balanced, on 100-Ω twin-axial cable or two 50-Ω coaxial cables

5. Mory, R., et al., "Development and Production of Multi-Gap Loop (MGL) Series EMP B-Dot Sensors," AFWL-TR-70-153, Kirtland Air Force Base, NM, February, 1971.

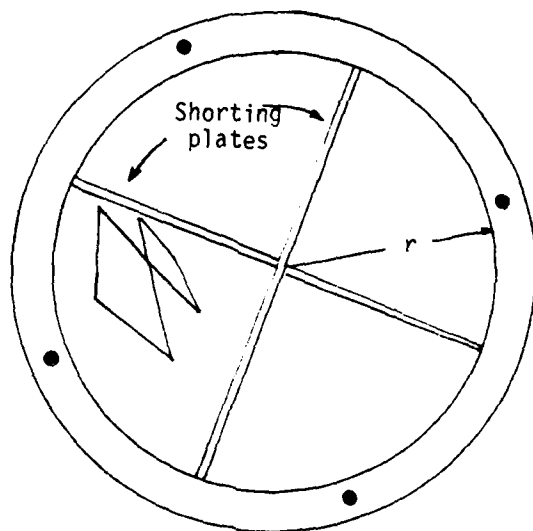


Figure 8. Internal view of MGL-2B (A) sensor (from Ref. 5).

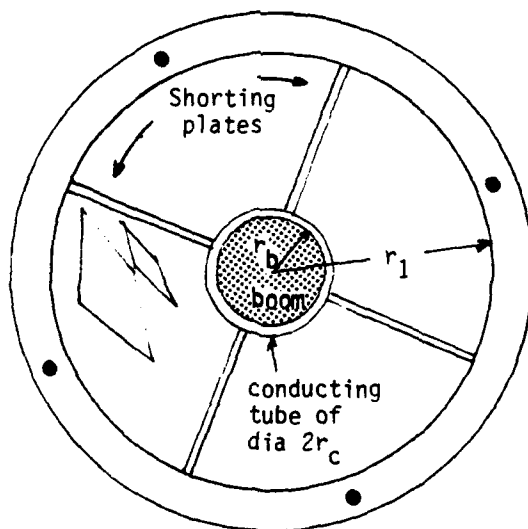


Figure 9. Internal view of proposed MGL-2E (AM) sensor accommodating the F-106B pitot-static boom. (Engineering drawings numbered B-82-136.05-01 to 05, which are available from the authors, show additional details.)

Although based on MGL-1A design, the smaller size led to a completely new construction technique (Ref. 5), by using a single printed circuit board for the conducting loop gaps and 200- Ω transmission lines. There are two 200- Ω strip transmission lines in each quadrant paralleled to yield a 100- Ω coaxial line (one per quadrant). The diagonally opposite gaps (1 and 3) and (2 and 4) can then be combined, resulting in two 50- Ω coaxial cables coming out of the sensor (e.g., UT-141 manufactured by Uniform Tubes, Inc., with an outer conductor dia. of 0.141" \pm 0.001"). For complete details see engineering drawings B-82-136.05-01 through -05, available from the authors.

Concerning the equivalent area, in the MGL-2B (A), the radius r of the copper surface of the printed circuit board = 0.083 m (3.265") which after due corrections for cross-sectional areas of divider plates, coaxes, and remaining hardware, results in $A_{eq} = 0.01 \text{ m}^2$. (See Figure 8).

The MGL-2B (A) sensor must be modified so that it may be slid onto the boom and attached securely. This is proposed in the following way. The center of the sensor must be bored out. A conducting tube must be inserted for structural integrity and to ensure that the shorting plates inside the sensor make electrical contact. This is illustrated in Figure 10. The inside diameter $2r_c$ of the conducting tube should be just large enough to let the boom slide through snugly. The boom outside diameter $2r_b$ is 1.75 in. in the general area of interest. Figures 9 and 10 illustrate the geometry. The skirts that will be used for aerodynamic compatibility can also be used for securing the sensor to the boom. Four dielectric screws can be used to secure the skirt to the sensor, and then the skirt may be attached to the boom through another series of four screws. Existing screw holes can be used.

Concerning the equivalent area for the proposed MGL-2E (AM), if the radius of the copper surface r_1 is chosen to be the same as r (the radius of MGL-2B (A)), there will be a reduction in A_{eq} due to the cross-sectional area of the boom. In either case, the MGL-2E (AM) could be

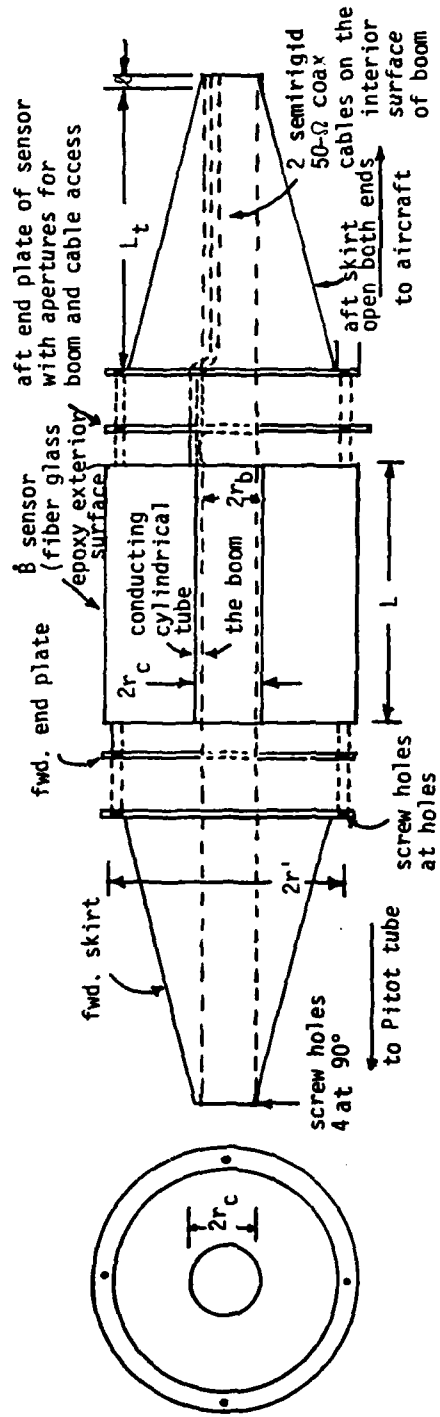


Figure 10. Design details of B-dot sensor [MGL-2E (AM)] based on available MGL-2B (A) data.

calibrated against a MGL-2B (A) sensor, in an experimental measurement of the same magnetic field, e.g., at the anechoic chamber facility at the radiation laboratory of the University of Michigan.

Concerning Figure 10, the radius r_c of the conducting tube should be chosen to permit a snug fit on the boom; and the end plate and taper should be made up of lightweight dielectric material, e.g., fiberglass.

4. PLACEMENT OF SENSOR

The radome and the pitot-static boom of the F-106B aircraft are illustrated in Figure 11. The proposed MGL-2E (AM) sensor will be placed in the general area of the α and β flow vanes, in a manner that does not obstruct or affect the pitot-static tube function. Four possible sensor locations are studied:

- OPTION 0 → Mid point of radome
- OPTION 1 → 2.895 m (= 9.5') forward of radome bulkhead
- OPTION 2 → 3.093 m (= 10.15') forward of radome bulkhead
- OPTION 3 → 3.29 m (= 10.8') forward of radome bulkhead

The position of the sensor corresponding to each option above is illustrated in Figure 12. The scattered field error estimates Δ_f , Δ_w , and Δ_h from Equations 3, 4, and 5, are computed, keeping in mind that the pitot-static boom is radially offset downward by an amount $\rho_0 = 0.15$ m (see Figure A3 in Appendix A) in the symmetry plane. Additional screw holes that need to be drilled in each case is determined. For example, in Option 1, the forward skirt of the sensor could make use of 4 existing screw holes, requiring 6 additional holes to be drilled, i.e., 4 for fastening the aft skirt to boom and 2 holes for sensor cable access into boom. Table 1 summarizes the qualities associated with all four options. In estimating the scattered field error estimates, the radius of the fuselage a is taken to be 1.07 m (42"), and radius of the sensing loop b is taken to be 0.086 m (3.4"). The radial offset of the sensor from the aircraft axis ρ_0 is

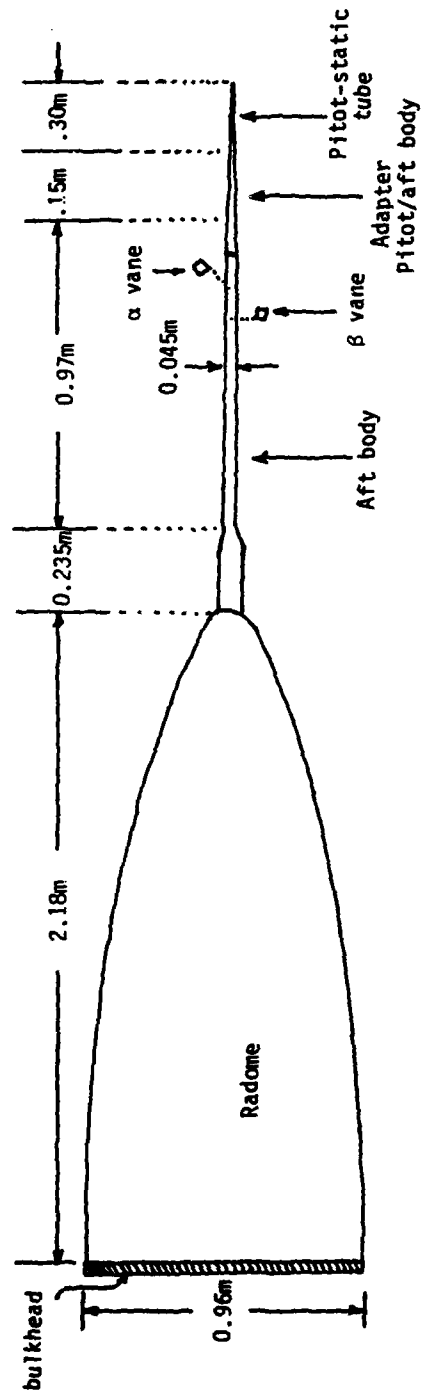
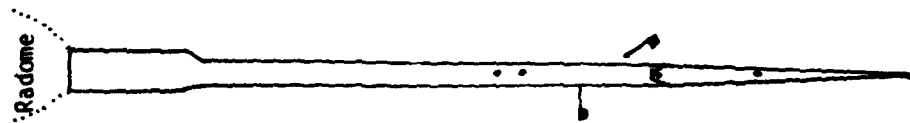
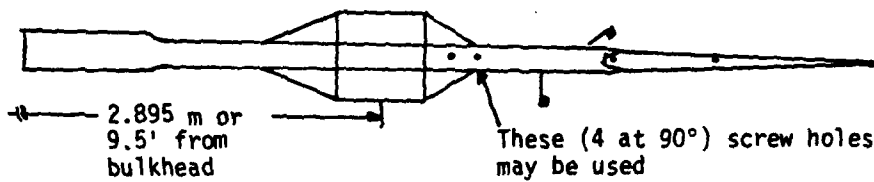


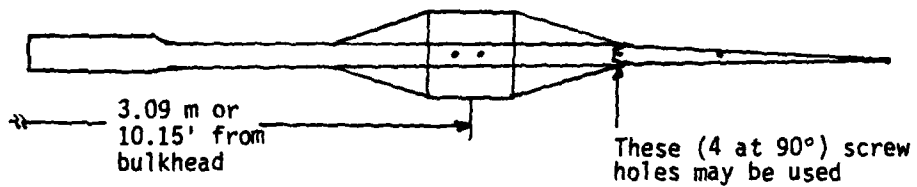
Figure 11. The radome and pitot-static boom on the F-106B aircraft.



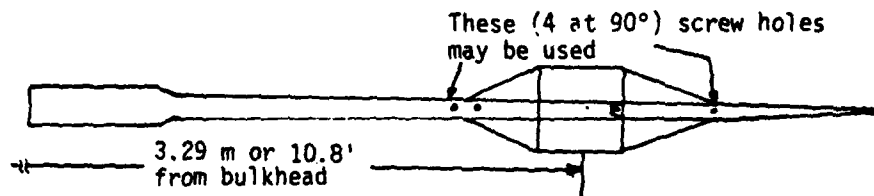
(a) Option 0 (sensor in radome)



(b) Option 1



(c) Option 2



(d) Option 3

Figure 12. Various options of sensor placement.

taken to be 0.15 m (6"). It was observed that Δ_f is sensitive to the offset ρ_0 . Several scatterer models were fitted to the aircraft. The best fit, which is in fair agreement with experimental scale model tests, attempts to fit the model accurately near the bulkhead region. All the options except Option 0 make use of available screw holes. Option 3 is recommended because of least error and the fact that it requires the least modification to the present boom. The major dimensions of the sensor for Option 3 are as follows:

- a. boom diameter $2r_b = 0.045$ m (1.75")
- b. conducting tube diameter $2r_c$ is chosen so it fits snugly on the boom, e.g., $2r_c = 0.046$ m (1.8")
- c. sensor radius to copper on printed circuit = 0.0829 m (3.265") if same material as MGL-2A is used, resulting in a reduction of A_{eq} of about 8%
- d. sensor radius to copper on printed circuit = 0.0858 m (3.38") to get $A_{eq} = 10^{-2} \text{m}^2$
- e. Length L of sensor = diameter of sensor
- f. Length of conducting tube = Length of sensor
- g. horizontal length L_t of skirts ≈ 0.0178 m (7")
- h. Length ℓ of flat portion of skirt (Figure 10) ≈ 0.006 m (0.25")

The above dimensions are approximate and have to be accurately measured out on the existing boom for proper fitting requirements.

The suggested installation procedure for mounting the sensor is given below.

- a. Slide aft skirt and end plate on to the existing boom.
- b. Mount forward skirt and end plate to sensor.
- c. Slide sensor unit onto boom, while aligning forward skirt to mounting holes.

- d. Feed sensor cables through aft end plate.
- e. Feed cables through apertures in boom to the instrumentation rack, while electromagnetically sealing them at boom entry.
- f. Attach aft end plate and taper to sensor.

It is estimated that there is adequate room in the boom interior to accommodate two UT-141 coaxial cables from the sensor, and it is anticipated that they can be accommodated through the current sensors in the radome.

TABLE 1. PHYSICAL QUANTITIES OF INTEREST WITH DIFFERENT POSITIONING OF THE MGL-2E (AM) B-DOT SENSOR.

#	OPTION CRITERION	0 In radome mid point	1 2.895 m from bulkhead	2 3.09 m from bulkhead	3 3.29 m from bulkhead
1 ^a	scattering error a. fuselage Δ_f b. wing Δ_w c. high freq Δ_h	20.7% 1.6% 40.0%	4.0% 1.2% 16.0%	3.6% 1.1% 15.0%	3.2% 1.0% 14.0%
2	Interference from Radar	Worst Case	Large	Medium	Least
3	Torque on Nose boom (around CG)	None	Least	Medium	Largest
4	Additional holes needed (see Figure 21)	None	6	6	2
5	Aerodynamic Compatibility	Not a problem	Good (Aerodynamic	Good testing could be done if needed)	Good
6	Skirt & Weight	No Skirts No added weight	Short Skirts Small added weight	Longer Skirt Greater added weight	Longer Skirt Greater added weight
7	Effect on α , β Vanes	No Effect	α , β Open	α , β Blocked	α , β Blocked

^a See Appendix A for details of this calculation.

III. EXPECTED B, B-DOT, AND SENSOR OUTPUT VOLTAGE DURING FLYBY

In this report dealing with the design of the proposed MGL-2E (AM) sensor, it is considered useful to compute the magnetic field B, its time derivation B-dot, and sensor output voltage $V_s = A_{eq} \times B\text{-dot}$ at some locations away from the VPD II facility. These computations are performed based on the equations in Reference 6, while accounting for a 10 ns rise time of the pulser. The magnetic field expression (Ref. 6) is given by

$$cB_{\phi}(\vec{r}, t) = \left[\frac{V_0}{2\pi f_g} \right] \frac{1}{r} \left[\epsilon_1'(\tau_h) + \frac{h}{r} \epsilon_2'(\tau_h) \right] \quad (6)$$

where

c \equiv speed of light = 3×10^8 m/s

$B_{\phi}(\vec{r}, t)$ \equiv time domain, azimuthal magnetic field

\vec{r} \equiv position vector with polar coordinates r and θ

t \equiv time

V_0 \equiv pulser voltage = 3.5 MV

f_g \equiv geometric factor = $\frac{1}{2\pi} \ln(\cot \frac{\theta_0}{2}) = (1/2\pi)$

θ_0 \equiv half angle of cone = 40.4 degrees

C_a \equiv antenna capacitance = $\frac{\epsilon_0 h_0}{f_g} \approx 2.21$ nF

ϵ_0 \equiv permittivity of free space = $[1/(36\pi \times 10^9)]$ F/m

6. Giles, J.C., Leib, J.C. and Sower, G.D., "Field Mapping Data for ATHAMAS II," ATHAMAS Memo 23, Air Force Weapons Laboratory, Kirtland Air Force Base, NM, March, 1979.

$h_o \equiv$ antenna height = 39.7 m

$C_g \equiv$ Marx generator capacitance = 5.4 nF

$t_r \equiv$ Pulser rise time = 10.0 ns (assumed)

$$\begin{aligned} \xi_1'(\tau_h, x) = & \sin \left[\frac{e^{-x\tau_h}}{\sin^2(\theta)} U(\tau_h) - \frac{[1+\cos^2(\theta)]}{\sin^4(\theta)} \left\{ \frac{1-e^{-x\tau_h}}{x} \right\} U(\tau_h) \right. \\ & + \frac{2 \cos^4(\theta/2)}{\sin^4(\theta)} \left\{ \frac{1-e^{-x(\tau_h-[1-\cos(\theta)])}}{x} \right\} U[\tau_h-1-\cos(\theta)] \\ & \left. + \frac{2 \sin^4(\theta/2)}{\sin^4(\theta)} \left\{ \frac{1-e^{-x(\tau_h-[1+\cos(\theta)])}}{x} \right\} U[\tau_h-1+\cos(\theta)] \right] \quad (7) \end{aligned}$$

$$\xi_2'(\tau_h, x) = \int_0^{\tau_h} \xi_1'(\tau_h, x) d\tau_h \quad (8)$$

A closed form expression for $\xi_2'(\tau_h, x)$ is available in Reference 6 and is not reproduced here. The parameter τ_h is given by

$$\tau_h \equiv \text{retarded time} = (ct - r)/h.$$

Also,

$$\xi_1'(\tau_h) = \xi_1'(\tau_h, \alpha) - \xi_1'(\tau_h, \beta)$$

$$\xi_2'(\tau_h) = \xi_2'(\tau_h, \alpha) - \xi_2'(\tau_h, \beta)$$

The pulser output is modeled by

$$V_p(t) = V_0(e^{-\alpha\tau h} - e^{-\beta\tau h}) \quad (9)$$

with

$$\alpha = 1 + (C_a/C_g)$$

$$\beta = \frac{2 \cdot 2}{t_r} \frac{h_0}{c}$$

The magnetic field $CB_\phi(t)$ in kV/m and its time derivative $\dot{B}_\phi(t)$ in kV/m² are computed at locations of interest for an upcoming flyby test near the larger VPD-II facility. These locations are illustrated in Figure 13, along with indications of \vec{r} , θ , θ_0 , ψ , and ϕ . Figures 14 to 21 show the computed $CB_\phi(t)$, whereas Figures 22 to 29 show the computed $\dot{B}_\phi(t)$ as well as the sensor pick-up voltage V_s (volts).

$\dot{B}_\phi(t)$ is computed by a numerical differentiation process of the computed $B_\phi(t)$ curves. The sensor pickup voltage is estimated for $\dot{B}_\phi(t)$, assuming an equivalent area A_{eq} of 0.01 m² for the B-dot sensor. From these computations, it is concluded that, at distances of interest for the flyby testing, there is adequate signal corresponding to the incident field.

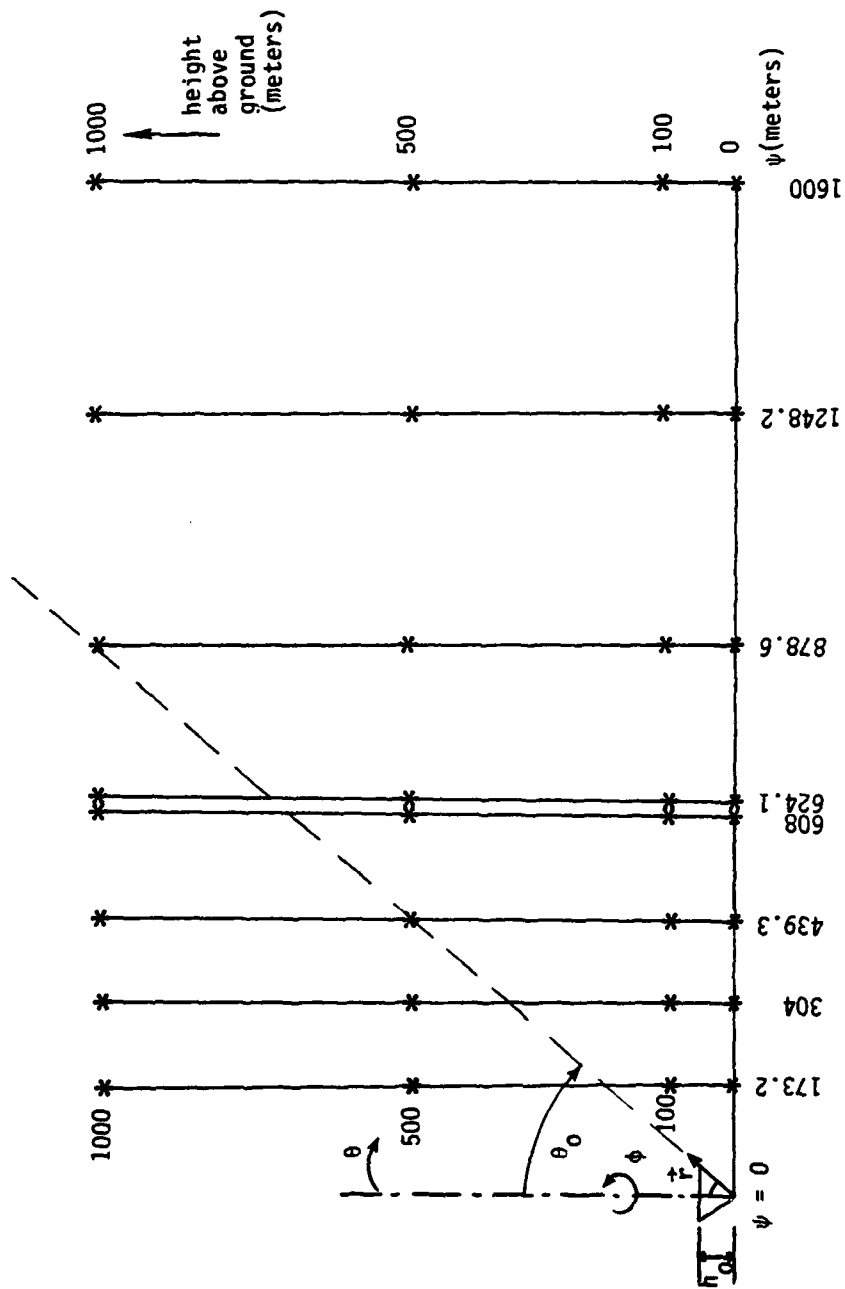


Figure 13. Locations used in computing cB_ϕ and B_ϕ for the VPD II facility.

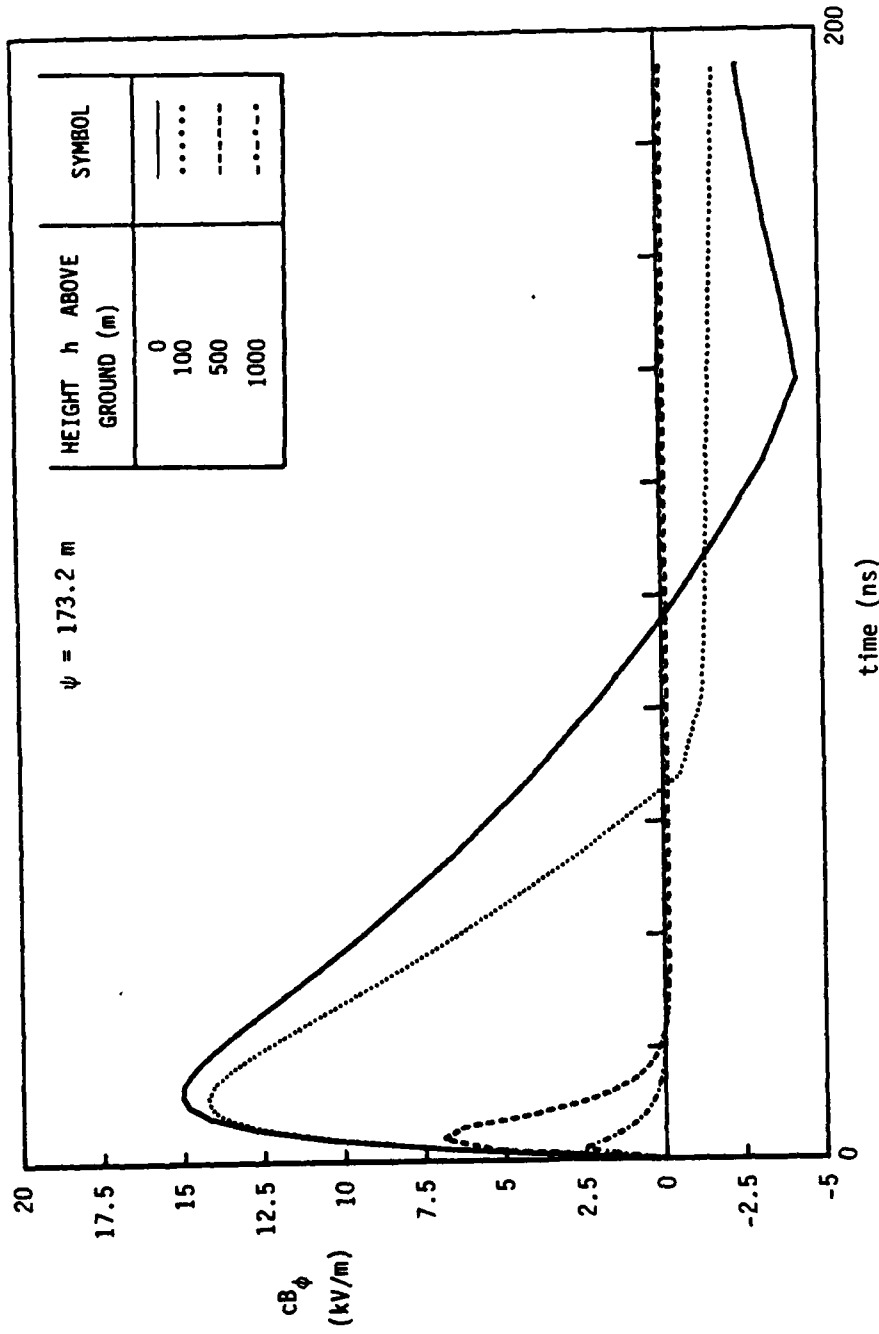


Figure 14. Computed cB_{ϕ} (kV/m) at different heights for $\psi = 173.2 \text{ m}$ from the VPD II apex.

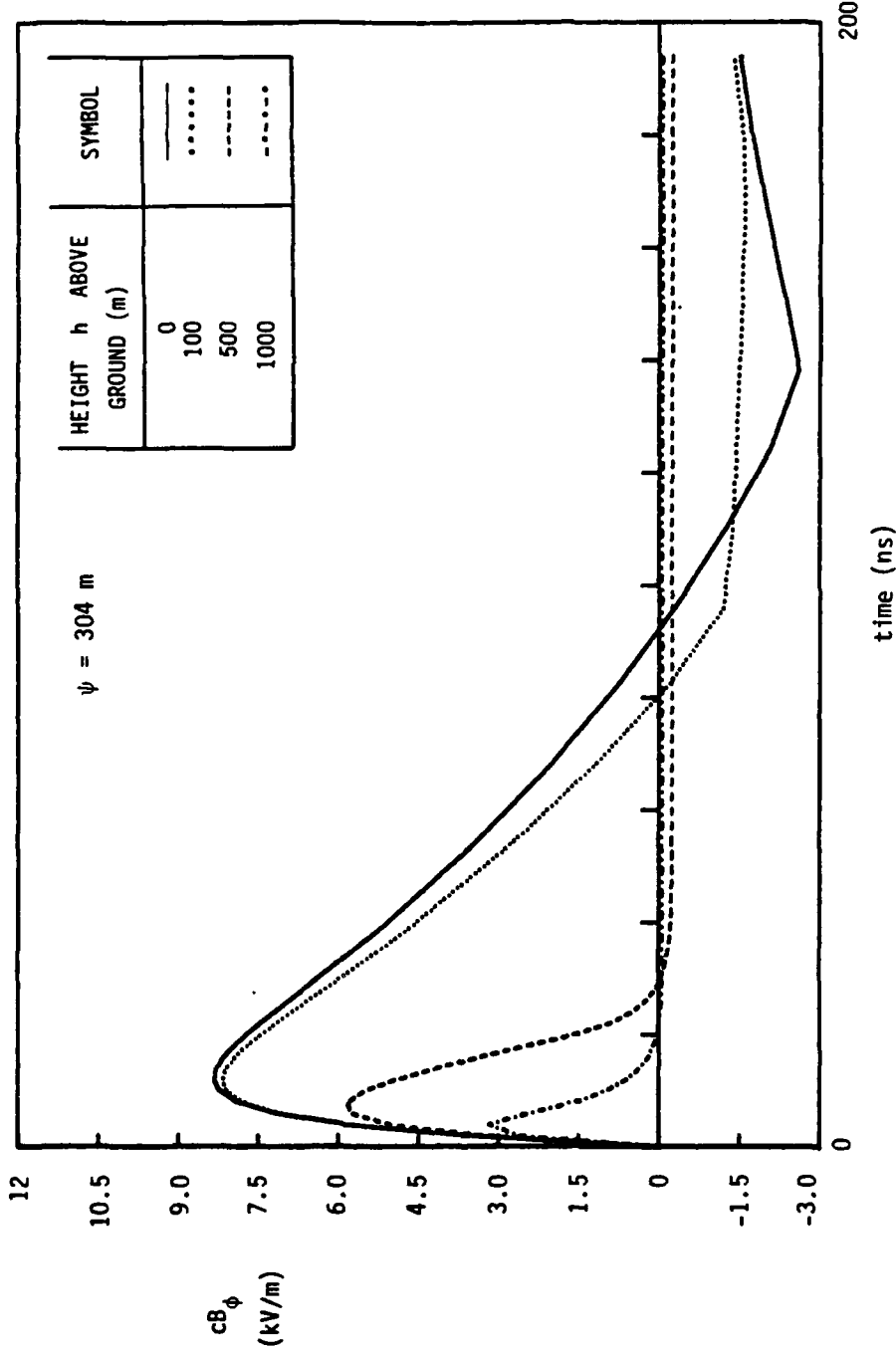
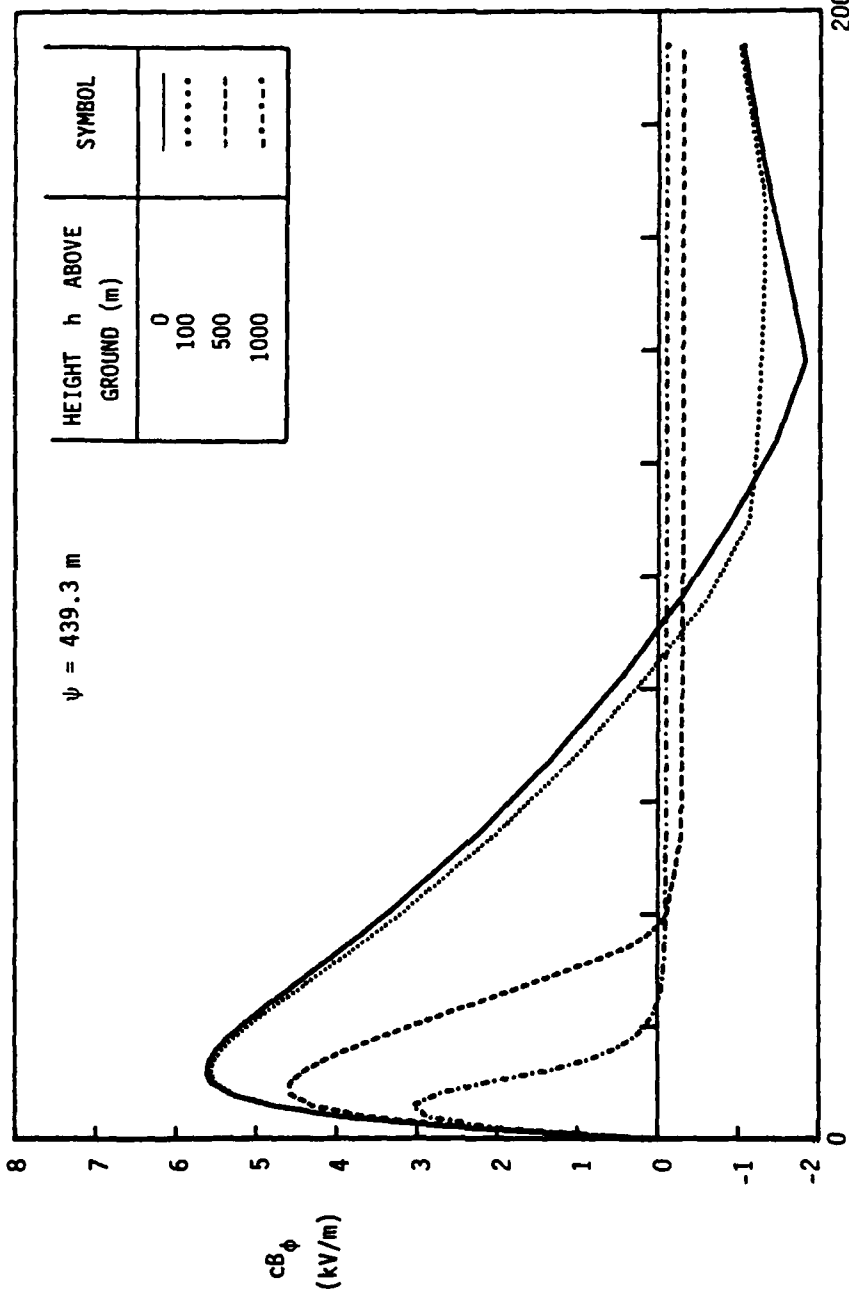


Figure 15. Computed cB_{ϕ} (kV/m) at different heights for $\psi = 304 \text{ m}$ from the VPD II apex.



200

Figure 16. Computed cB_{ϕ} (kV/m) at different heights for $\psi = 439.3 \text{ m}$ from the VPD II apex.

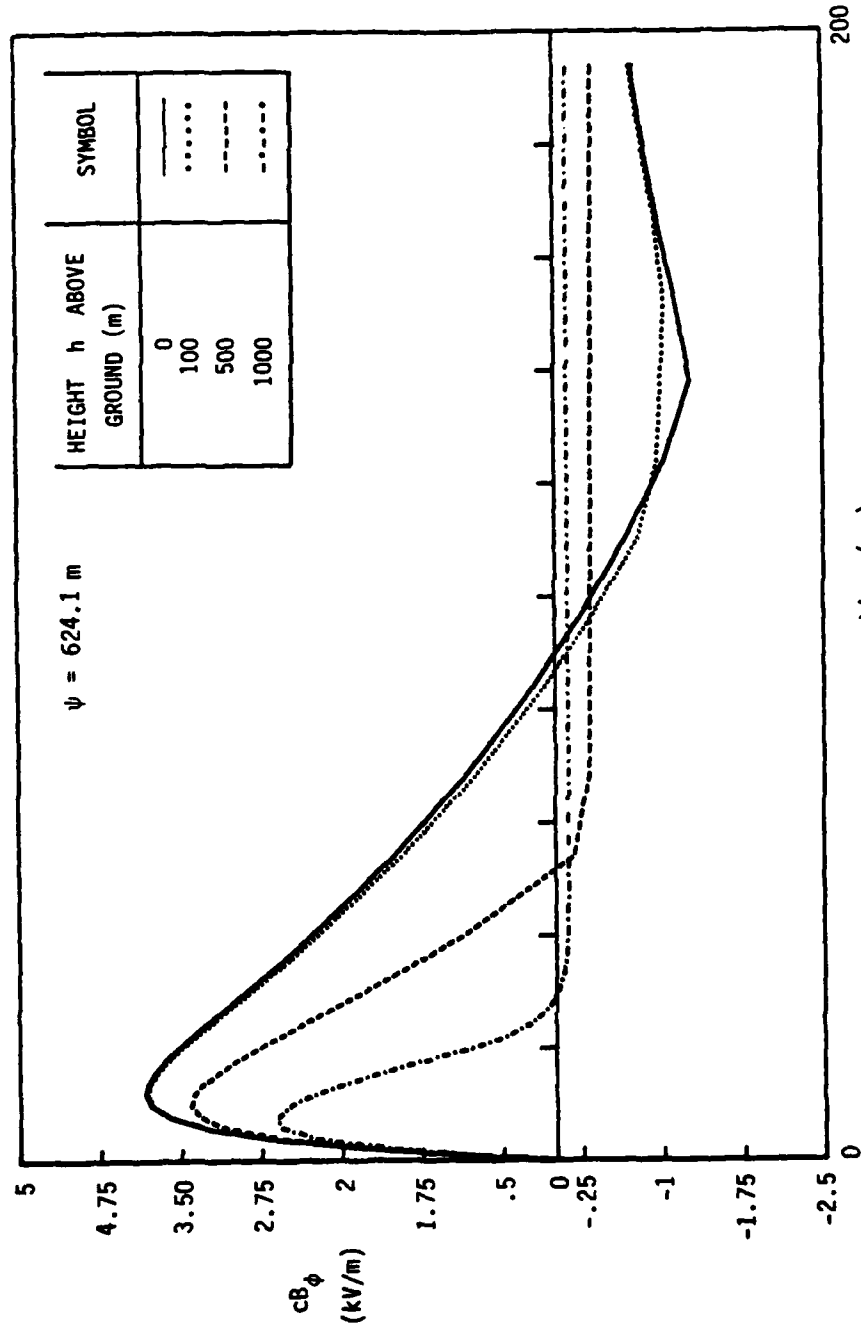


Figure 17. Computed cB_{ϕ} (kV/m) at different heights for $\psi = 624.1 \text{ m}$ from the VPD II apex.

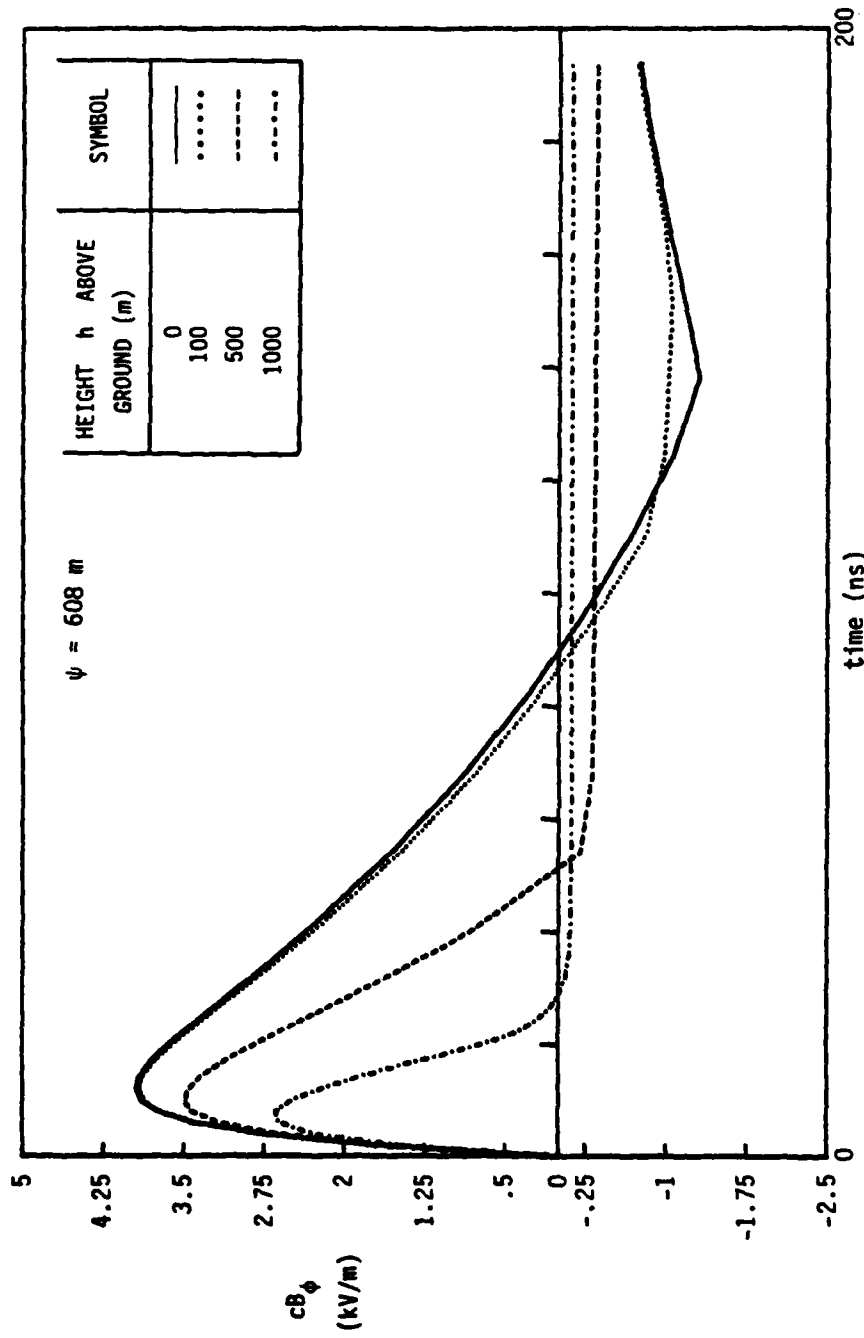


Figure 18. Computed cB_ϕ (kV/m) at different heights for $\psi = 608 \text{ m}$ from the VPD II apex.

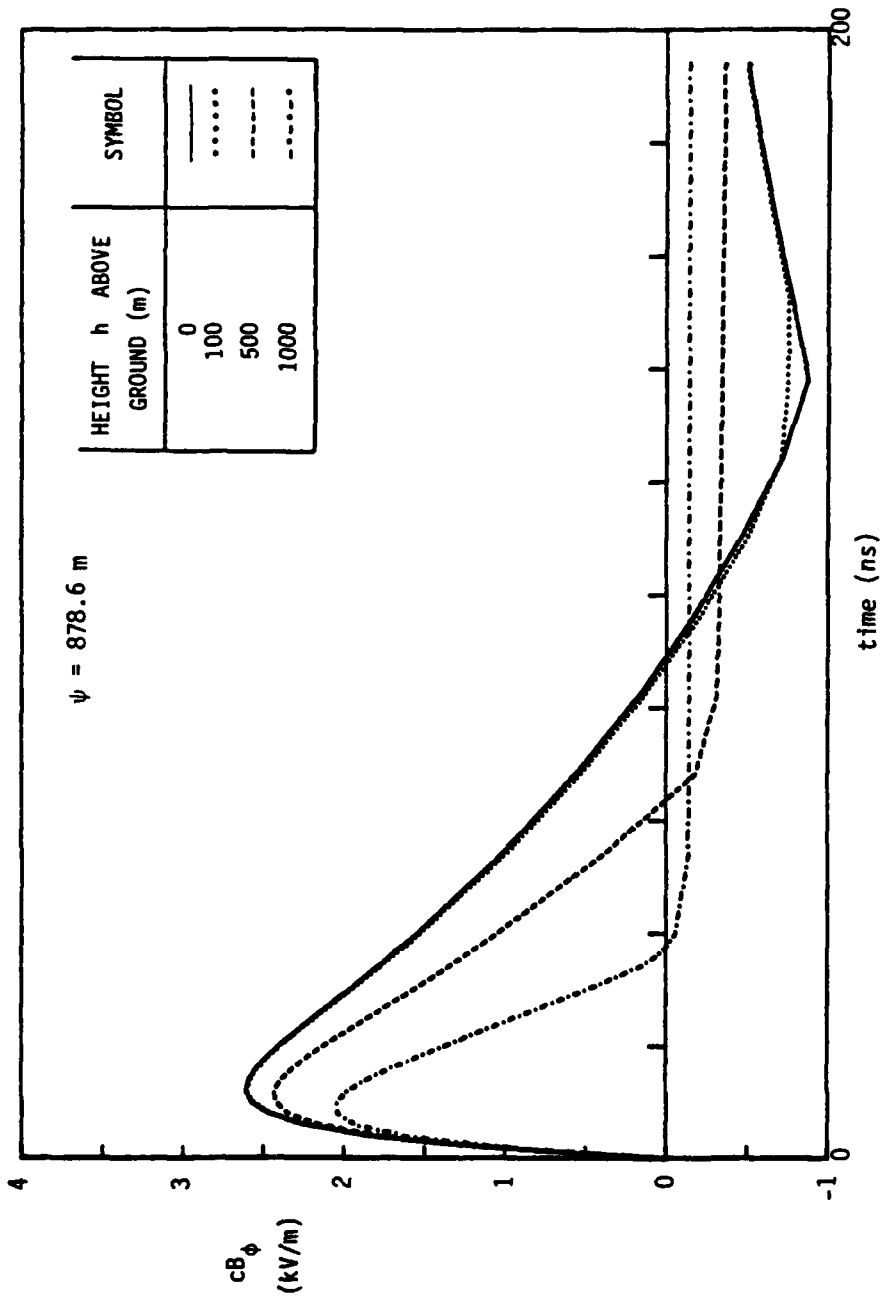


Figure 19. Computed cB_ϕ (kV/m) at different heights for $\psi = 878.6 \text{ m}$ from the VPD II apex.

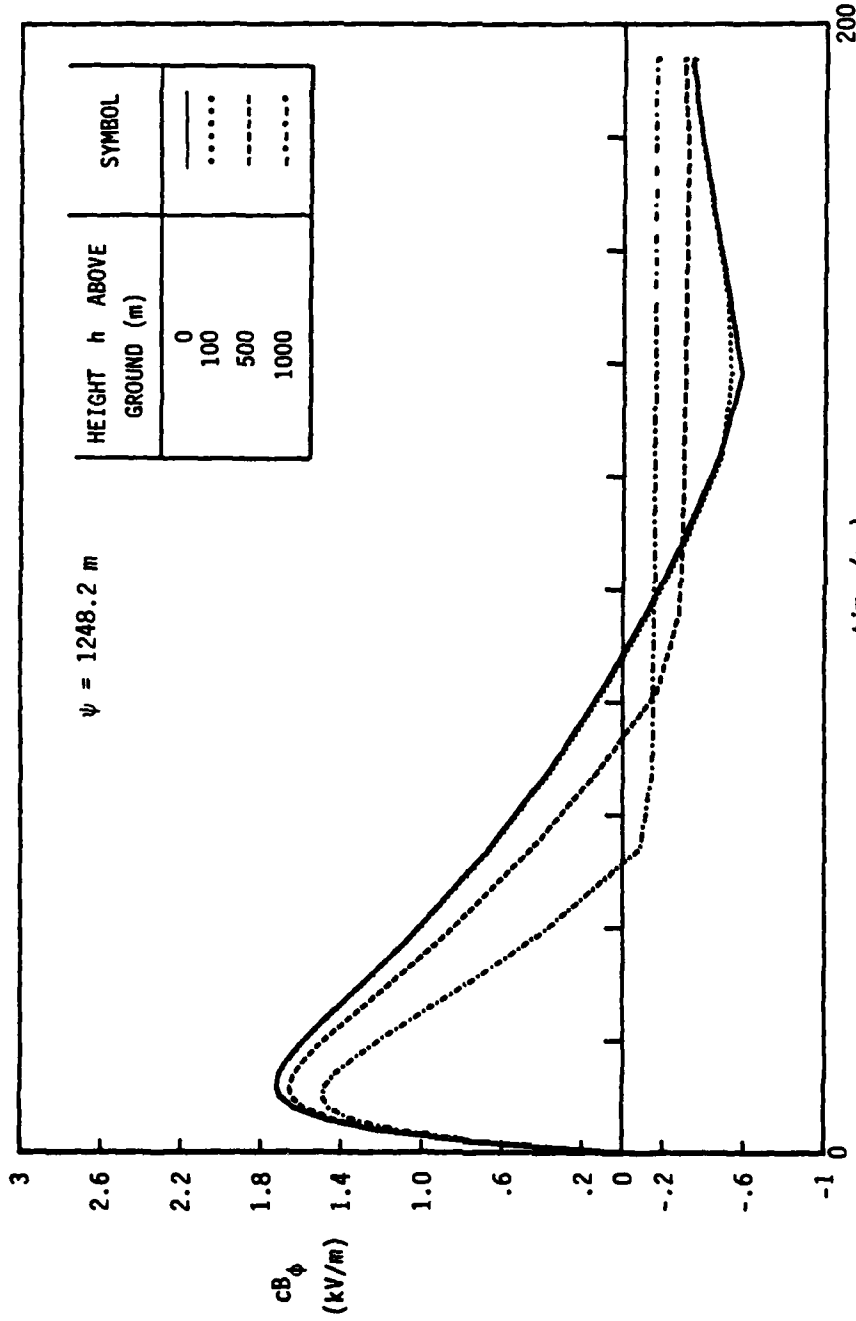


Figure 20. Computed cB_ϕ (kV/m) at different heights for $\psi = 1248.2 \text{ m}$ from the VPD II apex.

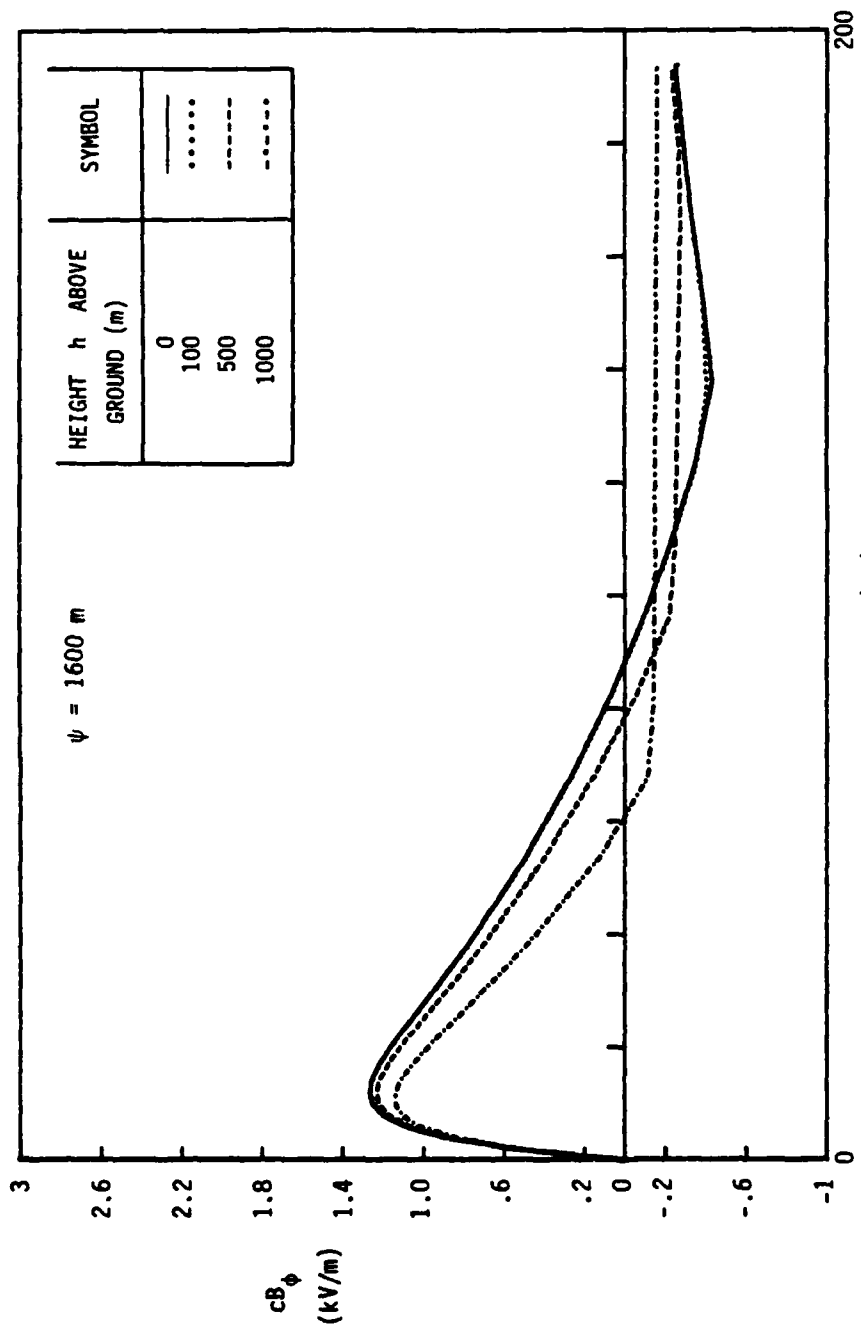


Figure 21. Computed cB_ϕ (kV/m) at different heights for $\psi = 1600 \text{ m}$ from the VPD II apex.

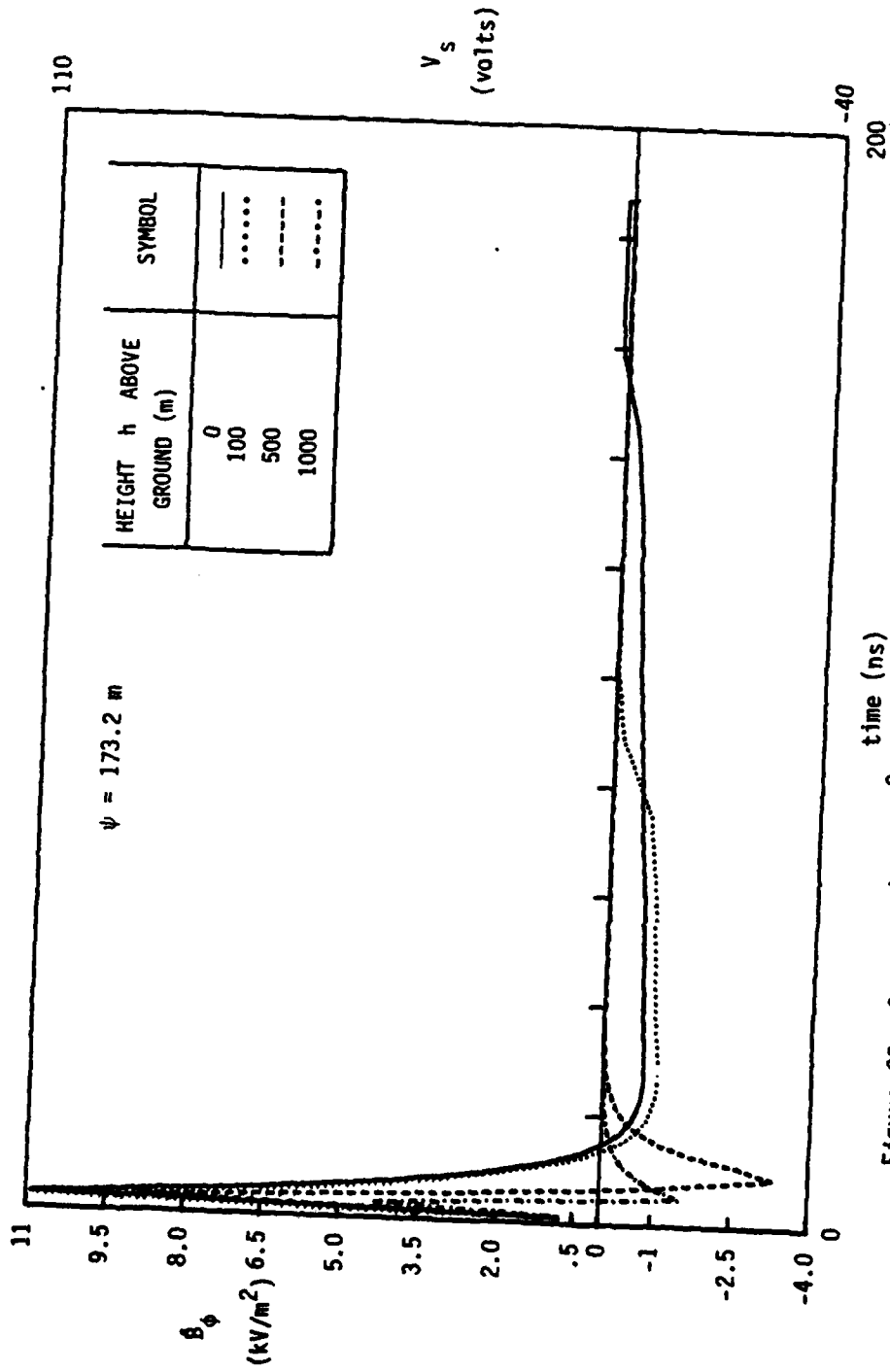


Figure 22. Computed β_ϕ (kV/m^2) and sensor output voltage V_s (volts) assuming $A_{eq} = 10^{-2} \text{ m}^2$ for a distance $\psi = 173.2 \text{ m}$ from the VPD II apex.

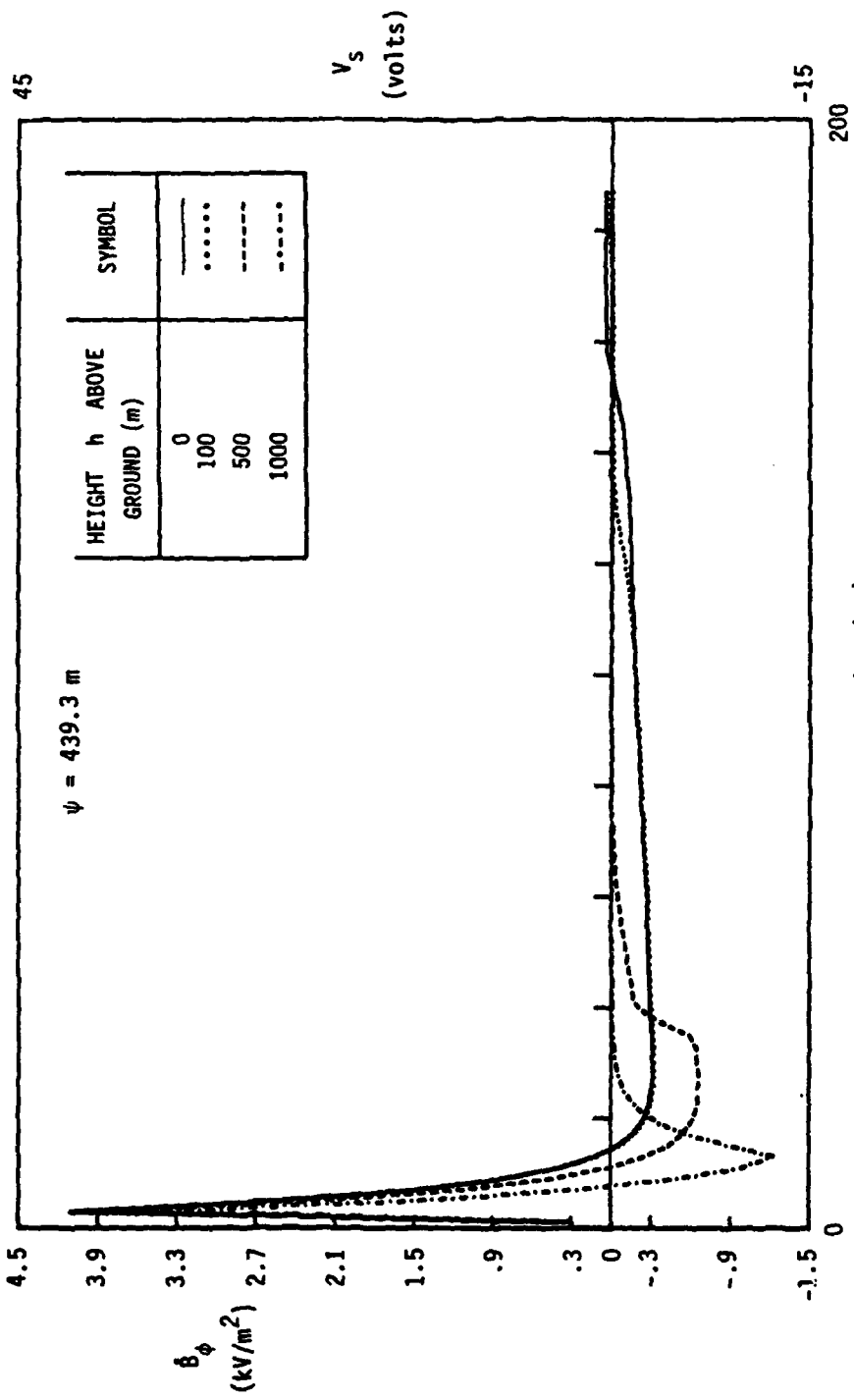


Figure 23. Computed B_ϕ (kV/m^2) and sensor output voltage V_s (volts) assuming $A_{eq} = 10^{-2} \text{m}^2$ for a distance $\psi = 439.3 \text{ m}$ from the VPD II apex.

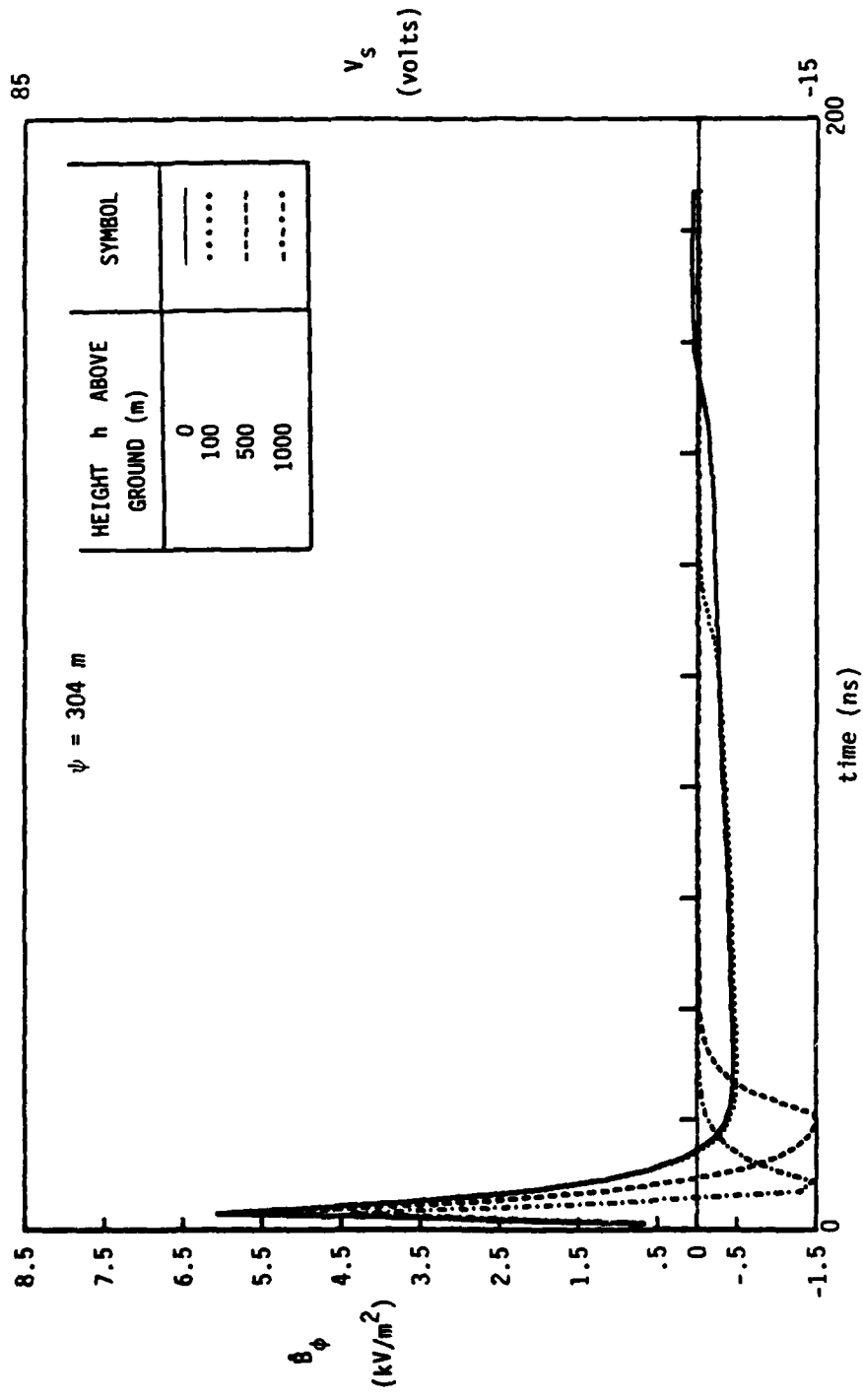


Figure 24. Computed E_ϕ (kV/m^2) and sensor output voltage V_s (volts) assuming $A_{eq} = 10^{-2} \text{m}^2$ for a distance $\psi = 304 \text{ m}$ from the VPD II apex.

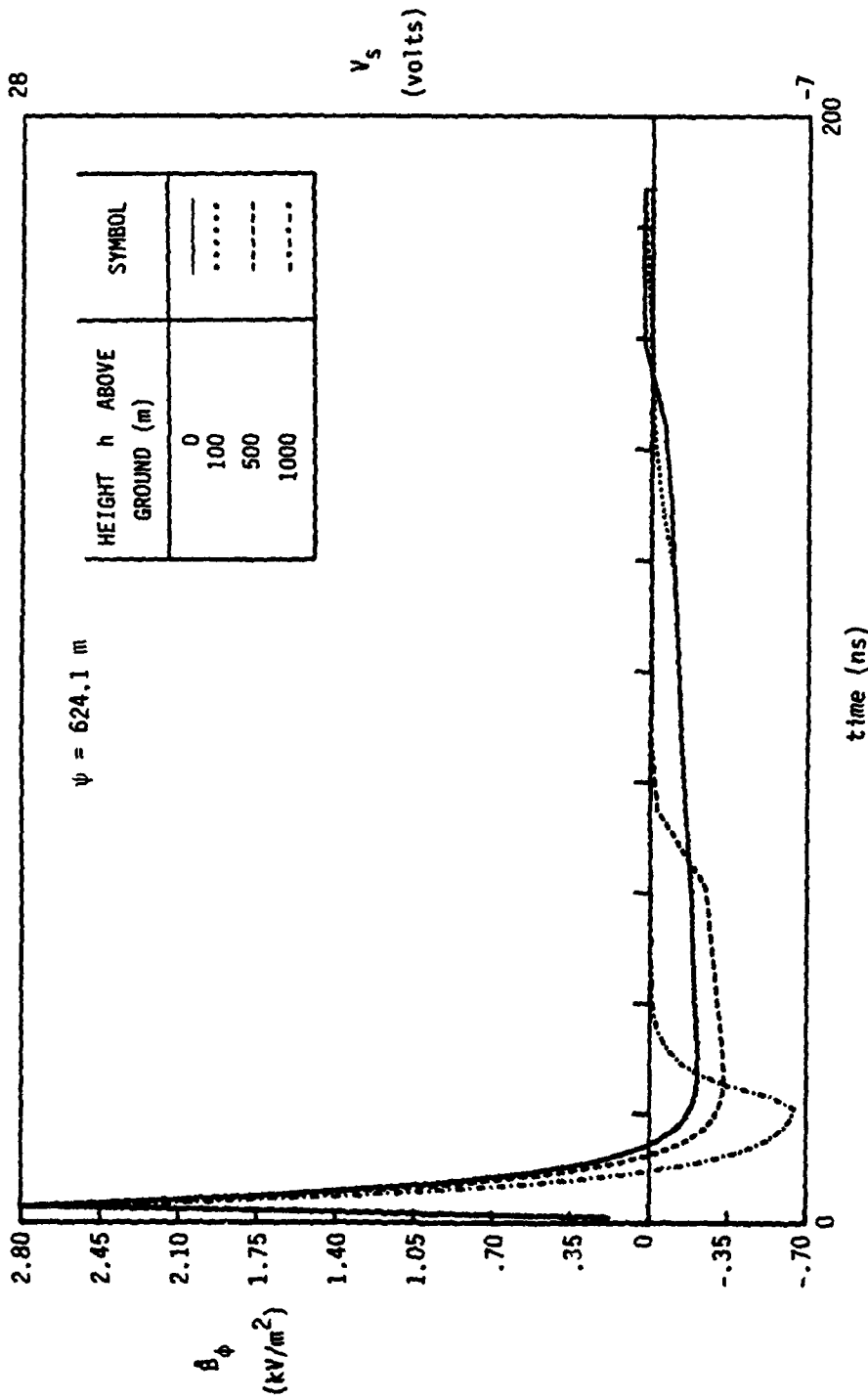


Figure 25. Computed \hat{b}_ϕ (kV/m^2) and sensor output voltage V_s (volts) assuming $A_{eq} = 10^{-2} \text{m}^2$ for a distance $\psi = 624.1 \text{ m}$ from the VPD II apex.

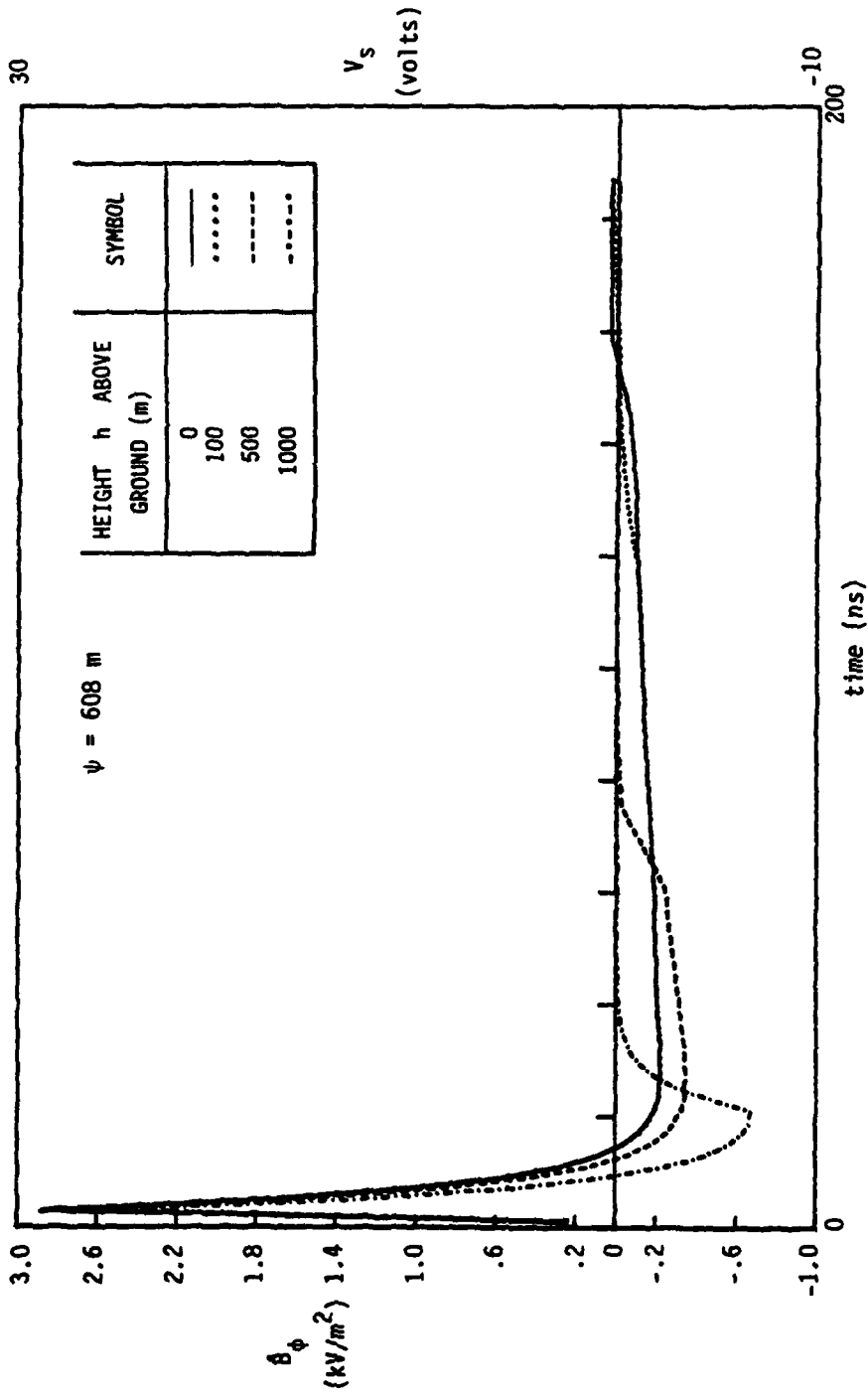


Figure 26. Computed δ_ϕ (kV/m^2) and sensor output voltage V_s (volts) assuming $A_{eq} = 10^{-2} \text{m}^2$ for a distance $\psi = 608 \text{ m}$ from the VPD II apex.

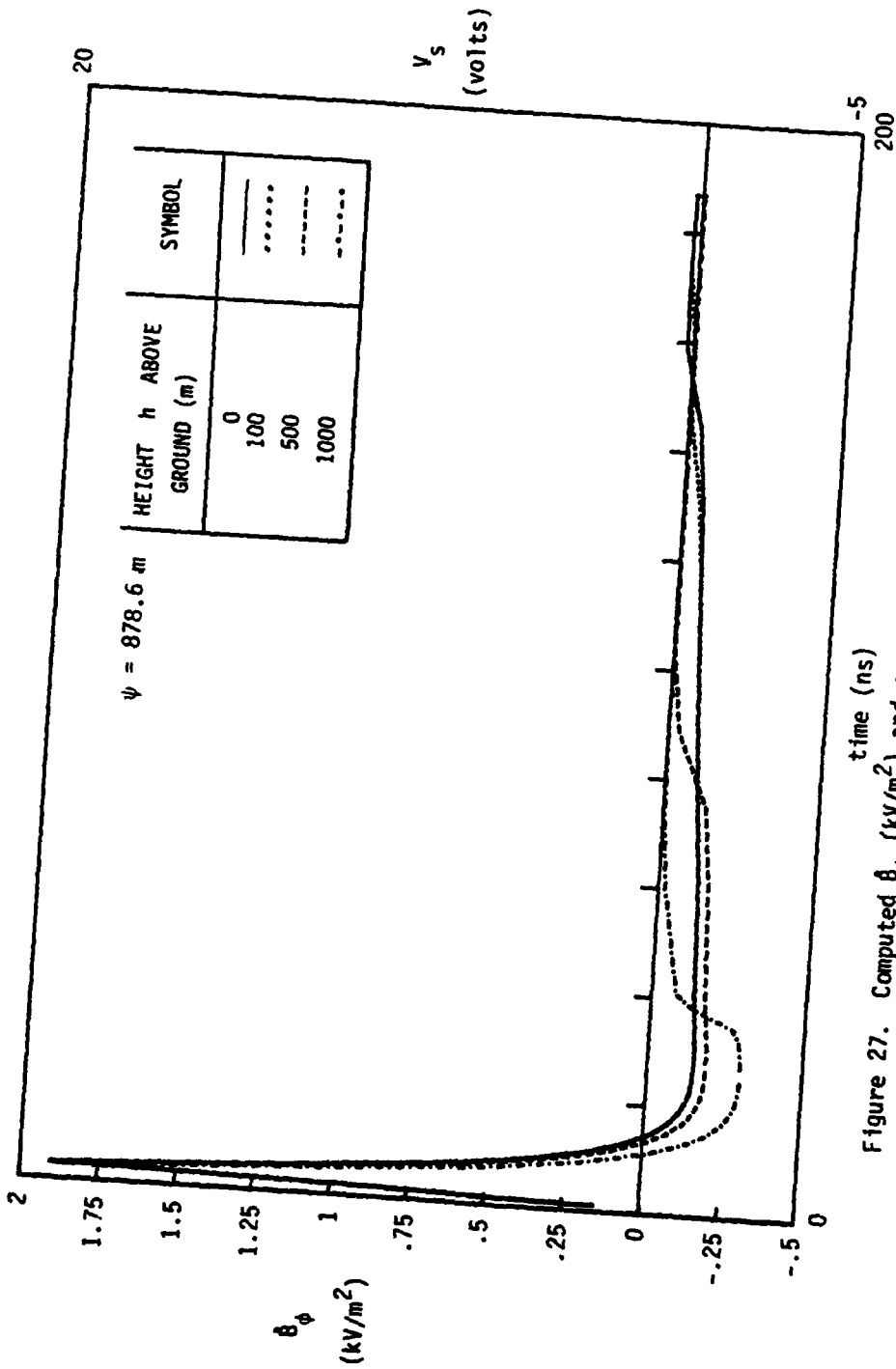


Figure 27. Computed β_ϕ (kV/m^2) and sensor output voltage V_s (volts) assuming $A_{\text{eq}} = 10^{-2} \text{ m}^2$ for a distance $\psi = 878.6 \text{ m}$ from the VPD II apex.

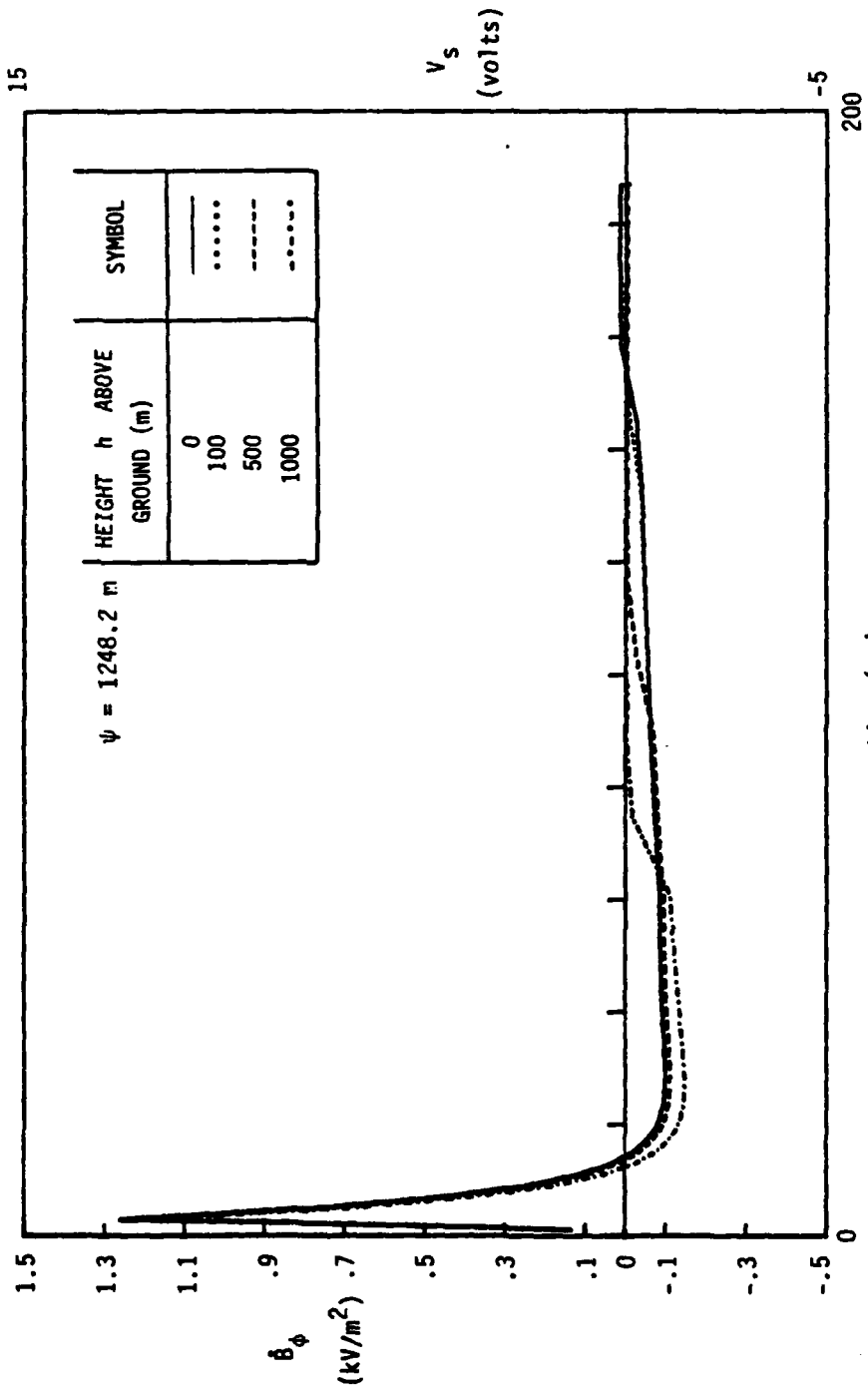


Figure 28. Computed B_ϕ (kV/m^2) and sensor output voltage V_s (volts) assuming $A_{eq} = 10^{-2} \text{m}^2$ for a distance $\psi = 1248.2 \text{ m}$ from the the VPD II apex.

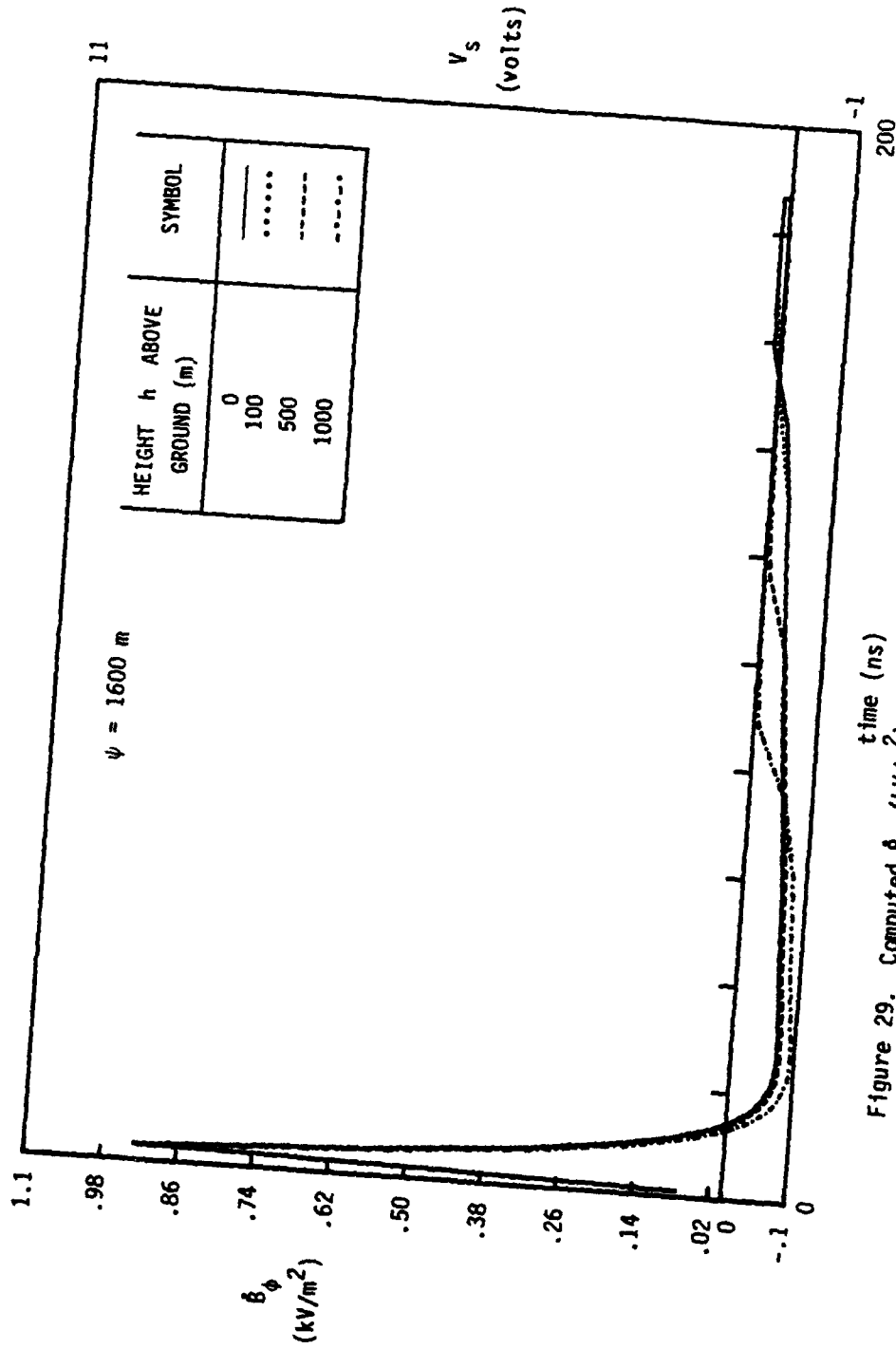


Figure 29. Computed δ_ϕ (kV/m^2) and sensor output voltage V_s (volts) assuming $A_{\text{eq}} = 10^{-2} \text{m}^2$ for a distance $\psi = 1600 \text{ m}$ from the VPD II apex.

IV. CONCLUSIONS AND RECOMMENDATIONS

From inspection of Table 1, it can be seen that option 3 would be the preferred location for the placement of the sensor. This is due to the lowest scattering error and the need for a minimal amount of modification to the boom itself. The detraction to this placement is the possibility of too much torque on the boom. If this is found to be the situation then option 2 would be the next preference. The placement of the sensor at the location of option 1 can also give satisfactory results if the other two locations prove not feasible due to torque on the boom. From Table 1, all three error estimates, i.e., scattered field pickup due to fuselage and wings and the high-frequency scattering errors, are within the experimental tolerances. In other words, options 1, 2, and 3 are expected to result in similar amounts of errors while measuring the incident magnetic field. However, for reasons stated above, options 3, 2, and 1 is the recommended ranking of the location for the incident field B-dot sensor placement.

Option 0, located inside the radome itself, would not be an acceptable location for the placement of the incident field B-dot sensor. The high frequency error is estimated at 40%, far too high for reliable measurements. The scattering error from the fuselage is over 20%. With such high values of error estimates, it is best to rule out option 0.

Selected data from scale model measurements performed at the University of Michigan are included in Appendix B of this report. In measuring the incident magnetic field from an airborne nose boom sensor, errors due to the sensor sensitivity to scattered fields from various parts of the aircraft are, to some extent, unavoidable. The scale model setup measures the fields with and without the aircraft and hence, error estimates are easily obtainable from such measurements. Preliminary analysis of the scale model experimental data has indicated that the errors are tolerable and that actual measurements of incident magnetic fields from airborne platforms should be possible.

In addition to the sensor design considerations, the incident field quantities $[B(t) \text{ and } \dot{B}(t)]$ were calculated for a number of different positions away from the VPD II. These positions correspond to the incident field measurement locations during the flyby tests at the VPD II facility, for assumed pulse parameters of 3.5 MV and a 10 ns rise time. From these calculations it has been determined that the sensor will be able to measure the incident magnetic field at all positions of interest during the flyby. In determining the sensor voltage, the equivalent area of the sensor is nominally taken to be 0.01 m^2 . After the flyby test is performed, the calculation of B and \dot{B} may have to be repeated with the exact pulser voltage and rise-time parameters. It is recommended that the nose boom sensor measurements with and without the aircraft on the test stand be made prior to flyby testing. Comparison of these two measurements, with a calculated incident magnetic field at the same location, will be useful in evaluating the sensor performance.

APPENDIX A
INVESTIGATION OF VARIOUS FUSELAGE SCATTERING MODELS

There are many ways to place the model for the quasi-magnetostatic fields scattered by the fuselage. No placement will entirely account for all the metal that contributes to the error in the B-dot measurement. Several model placements are considered here and their errors are calculated.

Figure A1 shows an analytical model fitted so that the larger rear diameter of the aircraft is taken into account. As can be seen, this placement introduces a large local error, i.e., the model represents a great deal of metal that does not exist close to the boom. The error generated by this model would not be expected to correlate well with experimental results.

Figure A2 represents another model fitting. In this case, the scattering model has been fitted with the aircraft diameter as viewed from the top. This model is quite different from the one in Figure A1, as can be seen from the top view of Figure A2. There is local error in this model also. In this case, however, the error is due to the lack of metal represented close to the sensor.

In Figure A3 is an attempt to more closely fit the local characteristics of the aircraft. In this model there is no excess metal, as in Figure A1, and not as much unaccounted for space as in Figure A2. With this model one would expect to get a truer representation of the actual scattering caused by the plane.

Figure A4 shows a model based on local fitting, as in Figure A3, but this time as viewed from the top. Due to the thinner cross section when viewed from the top, this model will generate a different error from that in Figure A3.

There are many more possible fittings that could be used to generate error estimations for the quasi-magnetostatic scattering. Those presented here encompass some reasonable choices.

The errors associated with each model are listed in Table A1. For each model, the error is calculated for each of the options presented in Table 1. $A(m)$ gives the distance from the bulkhead to the sensor. For the recommended option #, the error is Δ_f ; for the scattering models illustrated in Figure A2, A3, and A4, the error is below 4%. It appears that the scattering model of Figure A1 is inaccurate, given the low values of Δ_f observed in the scale-model experiments at the Radiation Laboratory of the University of Michigan, Ann Arbor. The results of the scattering model of Figure A3 are cited in Table 1 of this report. Some selected scale-model data provided by Professor Val Liepa of the University of Michigan are included in Appendix B.

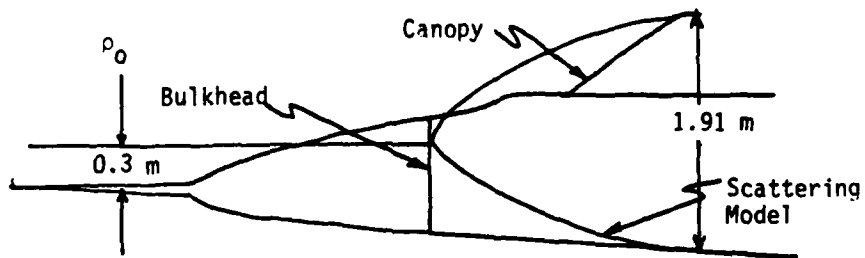


Figure A1. A model for quasi-magnetostatic scattering (side view).

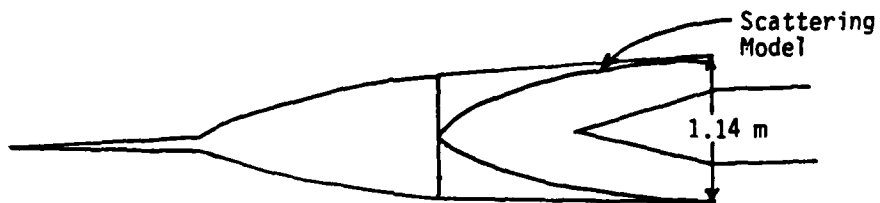


Figure A2. A model for quasi-magnetostatic scattering (top view).

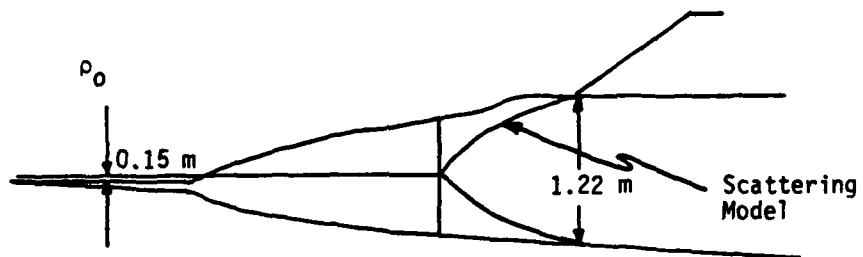


Figure A3. A model for quasi-magnetostatic scattering (side view).

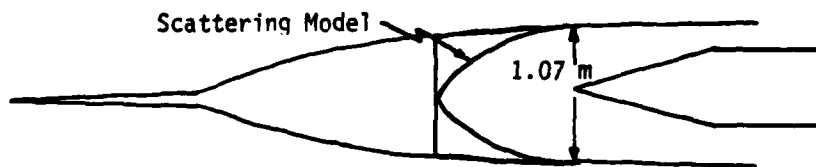


Figure A4. A model for quasi-magnetostatic scattering (top view).

TABLE A1. FUSELAGE SCATTERING ERRORS FOR THE DIFFERENT MODELS AND OPTIONS DISCUSSED IN THE TEXT.

FIGURE #	A(M)	ρ_0 (M)	OPTION #	SENSOR RADIUS (M)	Δ_F (%)
A1	0.96	0.30	0	0.09	69.2
	0.96	0.30	1	0.09	15.8
	0.96	0.30	2	0.09	14.1
	0.96	0.30	3	0.09	12.7
A2	0.57	0.08	0	0.09	12.1
	0.57	0.08	1	0.09	2.3
	0.57	0.08	2	0.09	2.0
	0.57	0.08	3	0.09	1.8
A3	0.61	0.15	0	0.09	20.7
	0.61	0.15	1	0.09	4.0
	0.61	0.15	2	0.09	3.6
	0.61	0.15	3	0.09	3.2
A4	0.54	0.08	0	0.09	11.1
	0.54	0.08	1	0.09	2.1
	0.54	0.08	2	0.09	1.8
	0.54	0.08	3	0.09	1.6

APPENDIX B
SELECTED DATA FROM SCALE-MODEL MEASUREMENT

To study the magnetic field coupling to a loop sensor in front of the airplane, for different illuminations, personnel at the Radiation Laboratory of the University of Michigan have performed scale-model measurements. Initially, the following illumination configurations were considered.

- a. Nose-on incidence with E parallel to wing and H parallel to vertical stabilizer
- b. Tail-on incidence with E parallel to wing and H parallel to vertical stabilizer
- c. Top fuselage-on incidence with E parallel to wing and H parallel to fuselage
- d. Bottom fuselage-on incidence with E parallel to wing and H parallel to fuselage

All of the above experiments could be and were performed by using a vertical ground plane. During the flyby, the H field is parallel to the fuselage and the E field is parallel to either the vertical stabilizer or the wings. Thus the flyby configuration of H parallel to fuselage and E parallel to wing with bottom fuselage-on incidence corresponds to case d above in the scale-model measurements.

Sample results of case a with the scale model are reviewed below. The measurement configuration is shown in Figure B1 and the location of nine observation points are shown in Figure B2. Figure B3 shows the experimentally measured field without the aircraft; $H_{iy} = 1$ is the incident field. H_{z0} is the axial field without the airplane (which should ideally be zero), but the measured quantity corresponds to noise level in the instrumentation. Figure B4 shows the measured axial magnetic field H_{z1} (which is due to scattering by the aircraft) at the central observation point. The amplitude of $[H_{z1} - H_{z0}]/H_{iy}$ is less than 0.1 (10%) at higher frequencies. At low

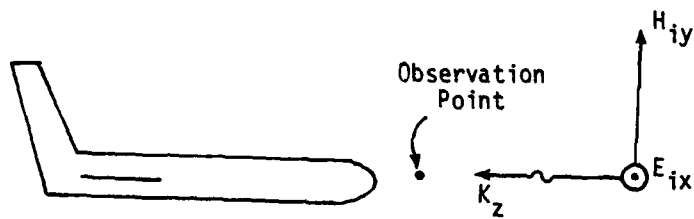


Figure B1. Nose-on incidence in scale-model measurements.

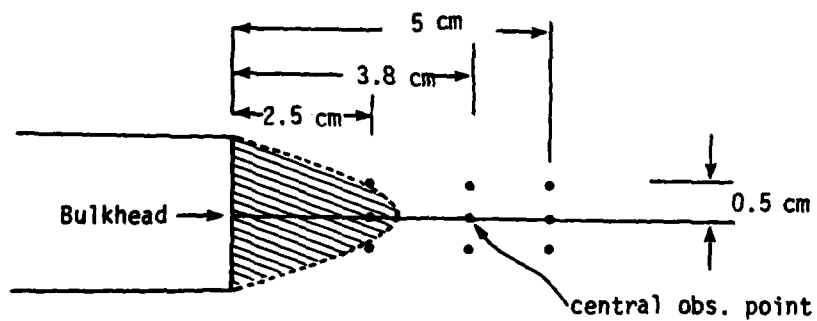


Figure B2. The observation points relative to bulkhead (the radome is removed during the scale-model measurements).

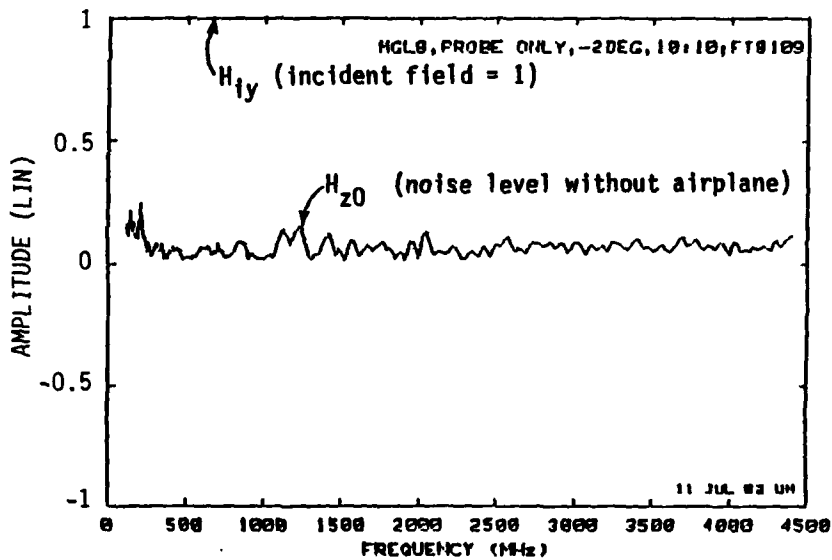


Figure B3. Measured field H_{z0} without the aircraft.

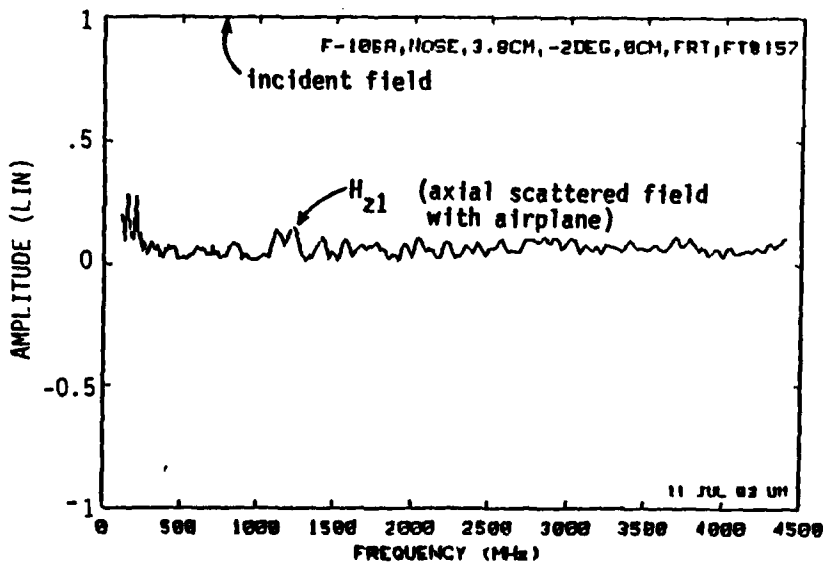


Figure B4. Measured field H_{z1} with the aircraft.

and resonant frequencies, the two curves, H_{z1} and H_{z0} (noise), match up and the deviation is at frequencies above the fourth harmonic of the principal fuselage resonance. At least for this configuration, it is reasonable to conclude that low and resonance frequency scattering due to antisymmetric wing currents can be eliminated from observation. However there is some amount of high-frequency scattered signal observed by the loop. A mean estimate of the error is defined by the following equation:

$$\epsilon_r = \frac{1}{N} \sum_{n=1}^N \left| \frac{V_1(f_n) - V_0(f_n)}{V_0(f_n)} \right| \quad (B1)$$

The mean error ϵ_r is estimated using the measured signals with (V_1) and without (V_0) the aircraft at sampled frequencies f_n . The angle θ between the fuselage axis and $-\vec{k}_z$ (negative direction of incident wave propagation) is varied. The $\theta = 0^\circ$ case corresponds to tail-on incidence, while $\theta = 180^\circ$ corresponds to nose-on incidence. The in-between angles of $\theta = \pm 10^\circ$ and 90° are also considered. From the measured fields with and without the aircraft, the mean error ϵ_r is estimated and shown in Figure B5. For all of the θ values, the electric field is exciting the wings, and when the sensing loop is oriented to pick up the magnetic field due to wing current, the maximum error estimates are less than 2.5 percent for both the nose-on and tail-on incidence.

The above measurements indicate that (1) the errors in the measured field are confined to high frequencies (above the fourth harmonic of principal resonance), and (2) even in the case of wing excitation, the errors are small and tolerable given the relative and proper orientation of the sensor with respect to the wing.

Additional experiments with variation of angle ϕ , between the direction of wave propagation and the plane of symmetry, were also performed. It is noted that angle θ is measured in the vertical plane, while ϕ is

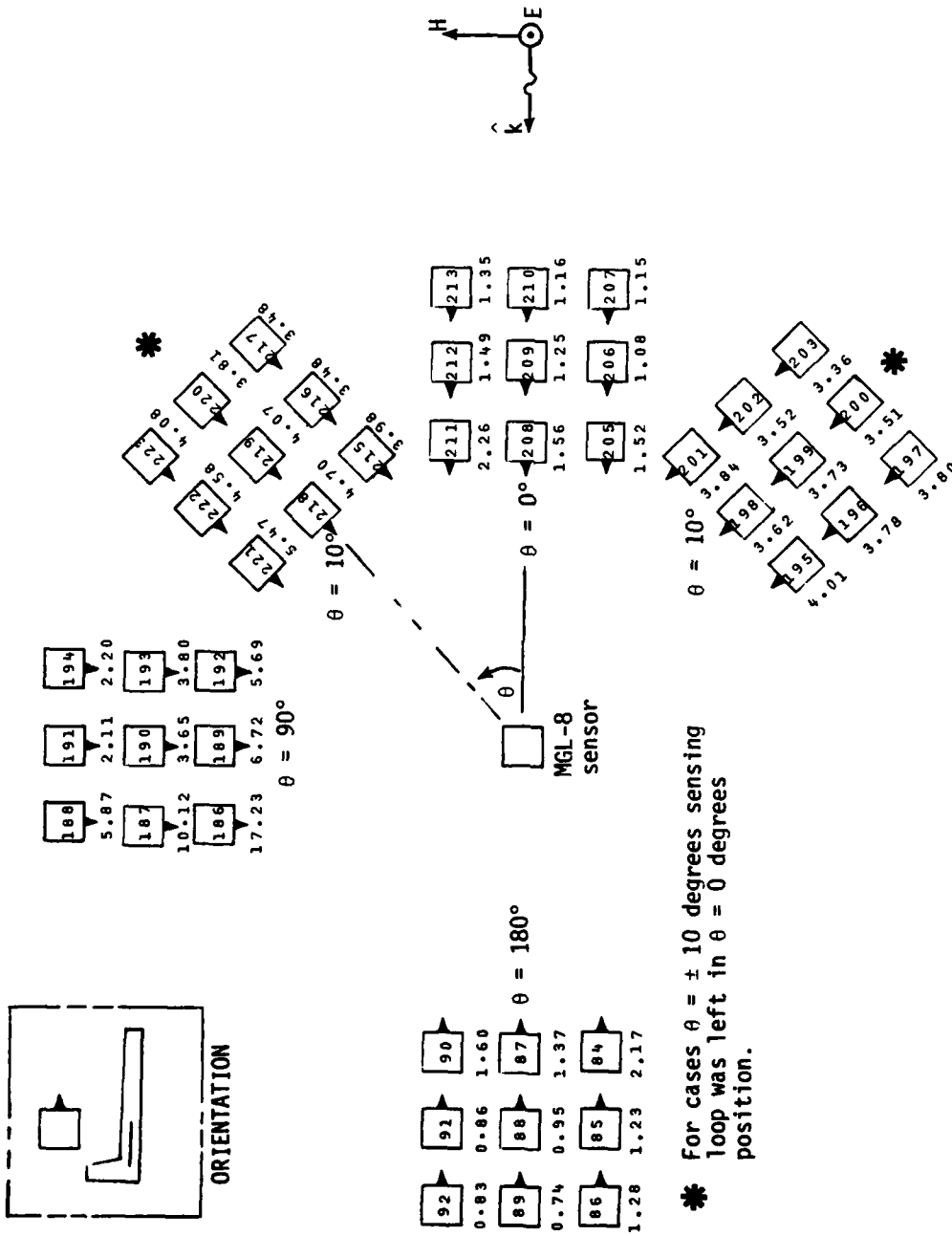


Figure B5. The error, ϵ_r , measured with a vertical ground plane oriented normal to the incident electric field. Boxed numbers indicate location numbers.

measured in the horizontal plane. Furthermore, since the majority of flyby testing, the incidence is from the right side of fuselage, so more experiments of the scale-model in free space were considered desirable. These free-space measurements were also performed. A summary of selected results from free-space experiments with close correspondence to actual flyby tests is presented here.

Figure B6 shows the position of test points in the free-space scale-model measurements. Two types of errors are defined as follows

$$E_1 = \frac{1}{N} \sum_{n=1}^N \left| \frac{V_1(f_n) - V_0(f_n)}{V_{ref}(f_n)} \right| \quad (B2)$$

$$E_2 = \sqrt{\frac{1}{N} \sum_{n=1}^N \left| \frac{V_1(f_n) - V_0(f_n)}{V_{ref}(f_n)} \right|^2} \quad (B3)$$

where V_1 , V_0 are sensor voltages with and without the model. V_{ref} is the voltage, with the sensor oriented to pick up the maximum magnetic field with no aircraft present.

Figures B7 and B8 show the results. The accompanying tables in these figures summarize the error results identified by the measurement positions, and the two error values E_1 and E_2 in percent. E_1 is the upper and E_2 is the lower figure. Note that the configuration of Figure B8 was also done with the use of a symmetry ground plane, and there the observed errors were half the measurements without the symmetry plane. This suggests that the free-space measurements are not as accurate, due to the interaction of the sensor leads on the measurement, etc.

Sensor location 5 of Figures B7 and B8 approximately corresponds to sensor location "OPTION 1" of Table 1 of this report. The measurements were made in the 118-4400 MHz range with a 1:72 scale model. The frequency

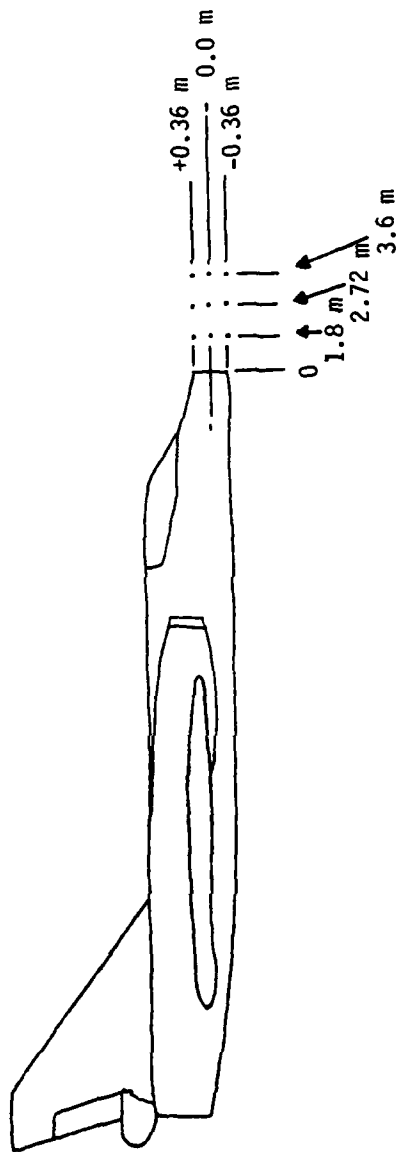
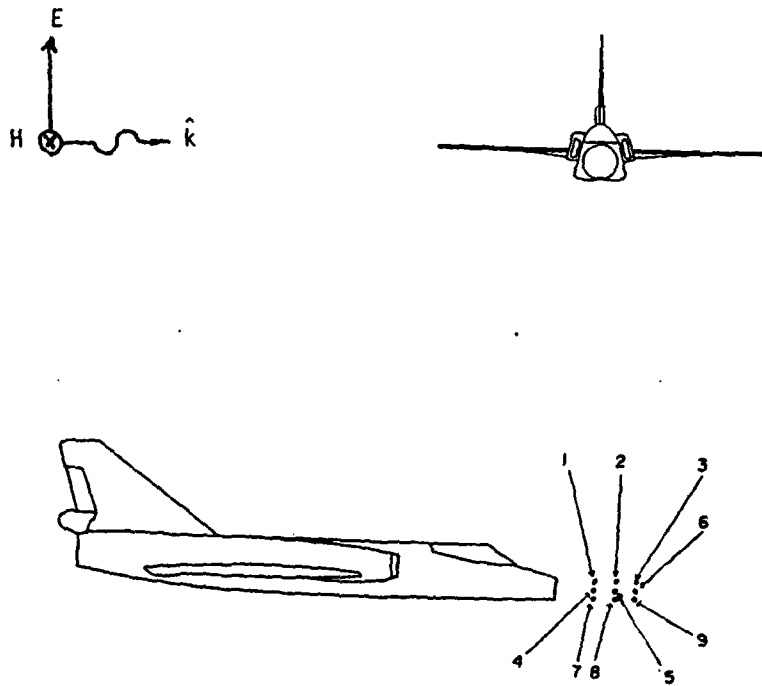


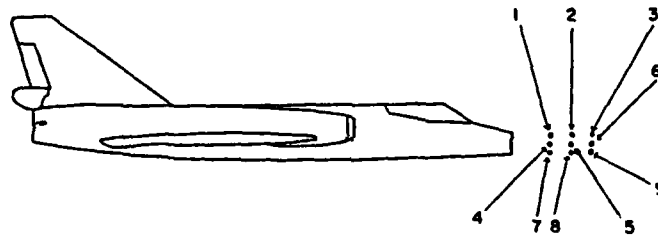
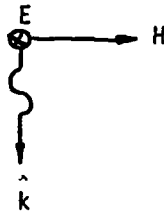
Figure 86. Position of the test points used in the scale-model measurements.



Measured Errors:

1	12.4	2	6.4	3	4.9
	13.6		8.2		6.6
4	14.5	5	6.7	6	4.9
	15.7		8.3		6.6
7	10.7	8	6.4	9	5.0
	10.2		8.2		6.7

Figure 87. Errors for right side incidence, E parallel to the vertical stabilizer. Errors E_1 and E_2 are in the upper and lower boxes respectively.



Measured Errors:

1	8.6	2	2.8	3	2.3
	9.4		3.2		2.6
4	11.1	5	2.6	6	2.2
	12.0		3.9		2.6
7	6.0	8	3.1	9	2.3
	6.5		3.5		2.6

Figure B8. Errors for top incidence, E perpendicular to the fuselage. Errors E_1 and E_2 are in the upper and lower boxes respectively.

range is 1.6 to 61 MHz on full-scale, and covers up to roughly eight times the principal fuselage resonance. At Option 1 location, the predicted high-frequency error is about 16% and predicted low-frequency errors are about 4%. The measured errors average out the frequency variation and a direct comparison is not possible. Since individual plots of measurements versus frequency are available, such comparisons can be made. However, the average measured error at the approximate location of Option 1 is below 8.5%. Recalling that the free space measurements are somewhat less reliable than ground plane measurements, this number is very encouraging. Since Options 2 and 3 are even further out from the bulkhead, corresponding numbers there are even smaller.

Thus, the scale model experimental results support the predicted sensor locations Option 1, 2 or 3.

END

DATE
FILMED

7-84

DTIC